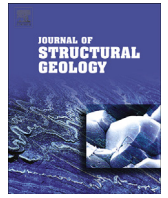




Contents lists available at ScienceDirect

Journal of Structural Geology

journal homepage: www.elsevier.com/locate/jsg

Deep permeability of the San Andreas Fault from San Andreas Fault Observatory at Depth (SAFOD) core samples[☆]

C.A. Morrow^{*}, D.A. Lockner, D.E. Moore, S. Hickman

U.S. Geological Survey, 345 Middlefield Road, MS 977 Menlo Park, CA 94025, USA

ARTICLE INFO

Article history:

Received 11 January 2013

Received in revised form

12 September 2013

Accepted 19 September 2013

Available online xxx

Keywords:

San Andreas Fault

SAFOD

Permeability

Fault gouge

ABSTRACT

The San Andreas Fault Observatory at Depth (SAFOD) scientific borehole near Parkfield, California crosses two actively creeping shear zones at a depth of 2.7 km. Core samples retrieved from these active strands consist of a foliated, Mg-clay-rich gouge containing porphyroclasts of serpentinite and sedimentary rock. The adjacent damage zone and country rocks are comprised of variably deformed, fine-grained sandstones, siltstones, and mudstones. We conducted laboratory tests to measure the permeability of representative samples from each structural unit at effective confining pressures, P_e up to the maximum estimated *in situ* P_e of 120 MPa. Permeability values of intact samples adjacent to the creeping strands ranged from 10^{-18} to 10^{-21} m² at $P_e = 10$ MPa and decreased with applied confining pressure to 10^{-20} – 10^{-22} m² at 120 MPa. Values for intact foliated gouge samples (10^{-21} – 6×10^{-23} m² over the same pressure range) were distinctly lower than those for the surrounding rocks due to their fine-grained, clay-rich character. Permeability of both intact and crushed-and-sieved foliated gouge measured during shearing at $P_e \geq 70$ MPa ranged from 2 to 4×10^{-22} m² in the direction perpendicular to shearing and was largely insensitive to shear displacement out to a maximum displacement of 10 mm. The weak, actively-deforming foliated gouge zones have ultra-low permeability, making the active strands of the San Andreas Fault effective barriers to cross-fault fluid flow. The low matrix permeability of the San Andreas Fault creeping zones and adjacent rock combined with observations of abundant fractures in the core over a range of scales suggests that fluid flow outside of the actively-deforming gouge zones is probably fracture dominated.

Published by Elsevier Ltd.

1. Introduction

Many models have been devised to describe the permeability and fluid flow characteristics of fault zones in an effort to address the long-standing discrepancy between heat-flow measurements, seismic stress drops, and the strength of crustal rocks (Lachenbruch and Sass, 1980, 1992; Hickman, 1991; Brune et al., 1969; Mount and Suppe, 1987; Zoback et al., 1987). For instance, Rice (1992), Byerlee (1990), Sibson (1992), Sleep and Blanpied (1992), Mase and Smith

(1987), and Faulkner and Rutter (2001) all invoke low-permeability regions within or adjacent to the actively-deforming fault core and fluid-pressure controlled fault weakening to explain the apparent weakness of the San Andreas Fault. Understanding fault-zone permeability structure is of paramount importance to these efforts. Permeability profiles across the Median Tectonic Line, Japan (Wibberley and Shimamoto, 2003), the Punchbowl fault, California (Chester and Logan, 1987), the Stillwater fault, Nevada (Caine et al., 2010), and the Carboneras fault, Spain (Faulkner et al., 2003) show that many fault zones, especially ones that have evolved with time, are more complex than the simple model of a low-permeability fault core bounded by high-permeability damage zones (e.g., Caine et al., 1996; Lockner et al., 2009).

The San Andreas Fault Observatory at Depth (SAFOD), located NW of the town of Parkfield, California, provides a unique opportunity to investigate the permeability of a seismically active, plate-bounding fault zone sampled at depth (Zoback et al., 2010). At Parkfield, slip on the San Andreas Fault (SAF) has brought

[☆] Peer-Review Disclaimer: This draft is distributed solely for purpose of scientific peer review. Its content is merely being considered for publication, so it is not to be disclosed or released by reviewers. Until the manuscript has been approved for publication by the U.S. Geological Survey (USGS), it does not represent any official USGS finding or policy.

^{*} Corresponding author. Tel.: +1 650 329 4824; fax: +1 650 329 5143.

E-mail addresses: cmorrow@usgs.gov (C.A. Morrow), dlockner@usgs.gov (D. A. Lockner), dmoore@usgs.gov (D.E. Moore), hickman@usgs.gov (S. Hickman).

dissimilar materials into contact. To the west of the fault lie Sainian granites and granodiorites, arkosic sandstones, and conglomerates, while to the east are found Cretaceous Great Valley Formation siltstones, mudstones and shales (Fig. 1a). The SAFOD borehole crossed the fault at a vertical depth of 2.7 km. An

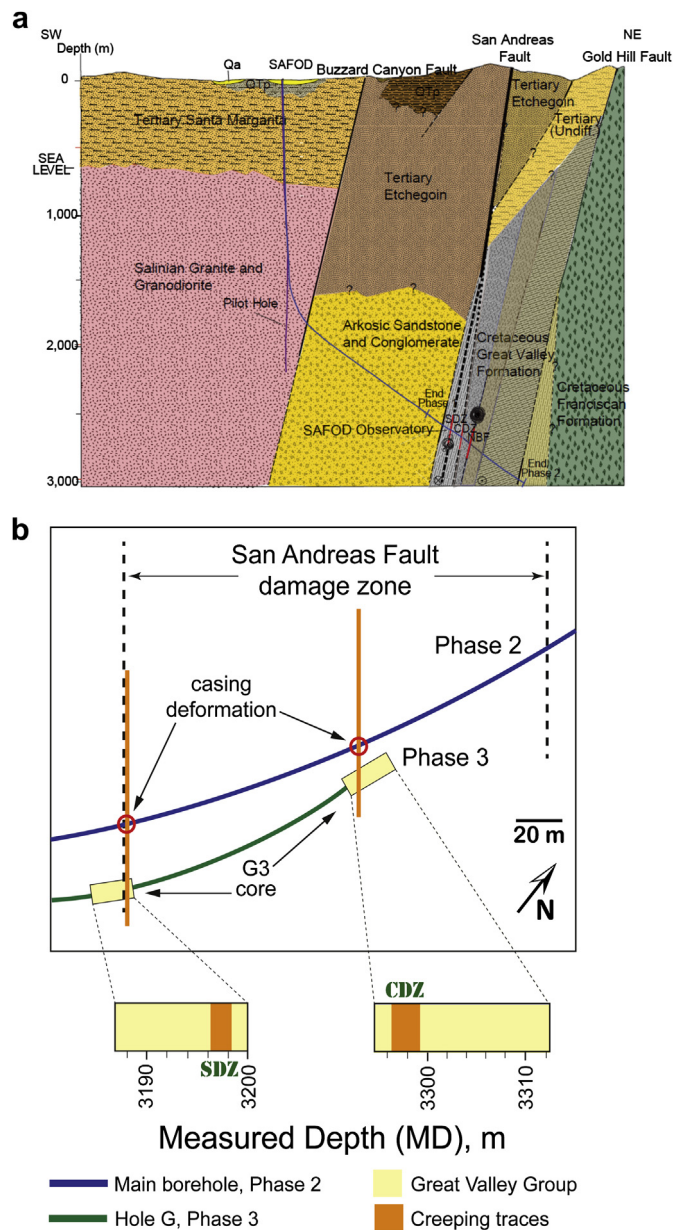


Fig. 1. a) A simplified geologic cross-section along the trajectory of the San Andreas Fault Observatory at Depth (SAFOD) borehole. The three prominent fault strands associated with the San Andreas Fault damage zone are shown in red. The southwest deforming zone (SDZ) and the central deforming zone (CDZ) are actively creeping faults identified through casing deformation. The damage zone is bounded by the SDZ and the northeast boundary fault (NBF). The black circles represent repeating micro-earthquakes. The depth at which SAFOD observatory instrumentation is deployed is shown. From Zoback et al. (2011). b) Map view of Phase 3 Hole G (green line) relative to the Phase 2 portion of the SAFOD main borehole (blue line). Coring targeted the SDZ and CDZ. Although SAFOD is drilled at a high angle to the San Andreas Fault Zone, the angle between the Hole G core axis and the SDZ and CDZ is not accurately known (see text). Modified from Fig. 1 of Lockner et al. (2011). (For interpretation of the references to colour in this figure legend, the reader is referred to the web version of this article.)

approximately 200 m-wide damage zone was encountered within rocks of the North American Plate (northeast side), which is characterized by anomalously low P- and S-wave velocities and low resistivity (Zoback et al., 2010, 2011). Observations of fault-zone guided waves in the SAFOD borehole show that this damage zone is laterally extensive and extends downwards to a depth of at least 7 km (Ellsworth and Malin, 2011). Two narrow, actively-deforming zones were identified within the damage zone based on borehole casing deformation. These actively-deforming zones, at 3192 and 3302 m measured depth (MD, depth as measured along the borehole) in the main Phase 2 borehole were the primary targets for coring during Phase 3 drilling in 2007. Phase 3 Hole G was drilled sub-parallel to the Phase 2 borehole and a total of ~30.7 m of core was recovered across the deforming zones at two depths roughly 100 m apart (Fig. 1b). (See Zoback et al., 2010, supplemental material, for a discussion of the correlation between measured depths in the Phase 2 and Phase 3 boreholes.) Two Mg-clay-rich gouge zones, referred to as the southwest deforming zone (SDZ) and the central deforming zone (CDZ), encountered in Hole G correspond to the two places identified in the Phase 2 borehole using repeat 40-finger caliper logs where the cemented steel casing was being deformed in response to fault creep. The CDZ takes up the majority of this active creep (Zoback et al., 2010). The northeast boundary of the San Andreas damage zone is defined by a narrow zone that has similar geophysical characteristics to the SDZ and CDZ. This zone is referred to as the northeast boundary fault (NBF) and is aligned with locations of the nearby repeating San Francisco and Los Angeles microearthquake clusters (Zoback et al., 2011). However, no casing deformation was detected on the NBF in any of the repeat caliper logs run from 2005 through 2007; thus, if this zone was creeping, it must have been at a relatively low rate. The two observed creeping strands are surrounded by variably deformed sedimentary rocks of the Great Valley Group (Fig. 2). See Bradbury et al. (2011) and Holdsworth et al. (2011) for descriptions of the lithology and internal structure of the recovered core sections.

In this study we present permeability measurements of axially oriented core (fluid flow in a direction parallel to the borehole axis) from the two Hole G cored intervals to relate the overall permeability structure of the SAF to rock type, mineral composition and rock strength. Sample locations and lithology are shown in Fig. 2 and discussed in more detail in Appendix 1. As mentioned above and discussed in more detail below, fault-zone permeability structure is expected to play an important role in determining pore pressure distribution and rates of fluid flow across and within the San Andreas Fault Zone. Our measurements show that, overall, matrix permeability is low throughout the damage zone and extremely low in the clay-rich actively-deforming zones.

2. Samples studied

Seventeen samples oriented parallel to the core axis were selected (black filled circles in Fig. 2), to obtain representative data for all of the major structural units. Measured depths in Hole G of these samples are reported in Table 1. Hole G is oriented at a slightly oblique angle (~80–90°) to the strike of the surface trace of the SAF, at an inclination of 52–62° from vertical at the depths from which the cores used in this study were obtained (see borehole trajectory for all SAFOD phases at <http://safod.icdp-online.org>). However, the strike and dip of the active strands of the SAF where cored by SAFOD are not well constrained, and the exact orientation of the core relative to the SDZ and CDZ is still a topic of ongoing research. For the purposes of the present study, this uncertainty in relative orientation should not be significant. Indeed, as we discuss

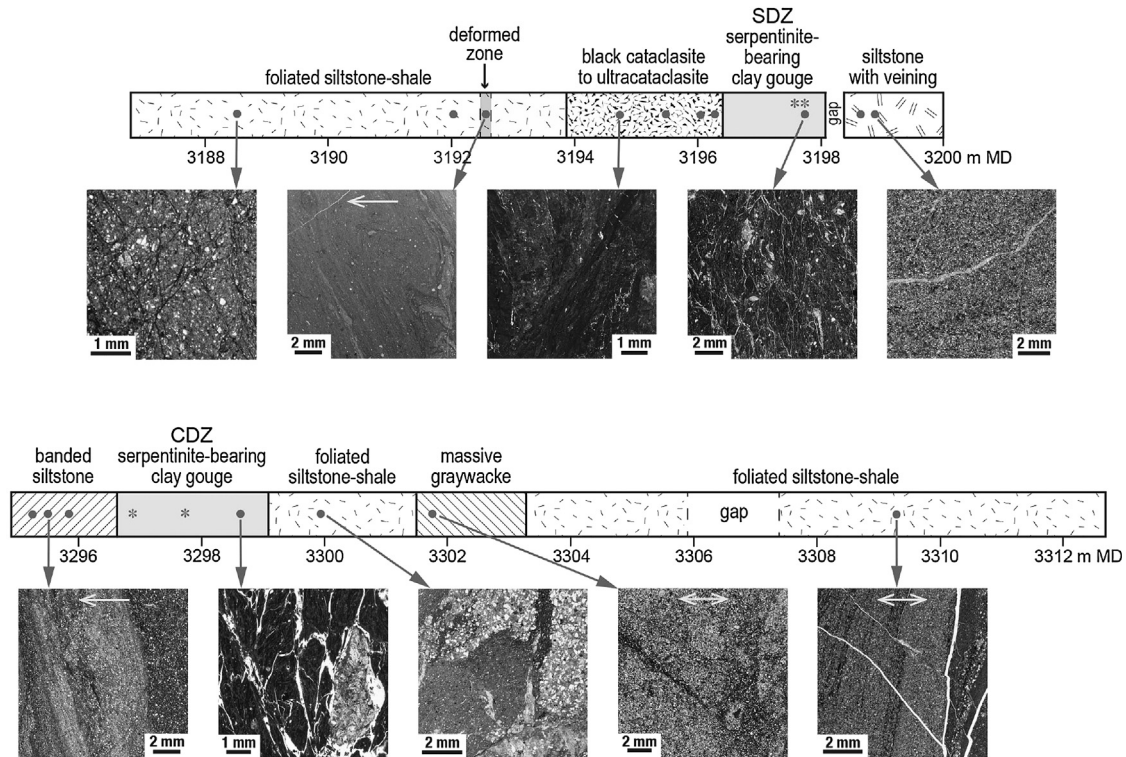


Fig. 2. Locations in Hole G of the intact (circles) and disaggregated (stars) samples tested in this study, plotted on the lithologic sections of Bradbury et al. (2011; their Fig. 2). Sample depths and physical property measurements are presented in Table 1. Portions of thin-section scans for ten samples illustrate textures representative of each structural unit. All but four of the thin sections were prepared from unoriented remnants from the sample-preparation process. For the oriented samples shown, a single-headed white arrow within the field of the photomicrograph indicates the “up” direction along the borehole axis, and a two-headed white arrow shows the orientation of the core axis (“up” direction unknown).

later, permeability anisotropy in the actively-deforming gouge material appears to be small, so that sample orientation of this material has little effect on measured permeability. Four additional, ground-up (disaggregated) samples from the CDZ and SDZ were tested (stars in Fig. 2); frictional strengths of these four samples are reported by Lockner et al. (2011). One SDZ sample (3197.7 m) was tested for permeability both as intact core and disaggregated material.

Portions of ten thin-section scans are included in Fig. 2 to illustrate some of the textural features of the core. Most of the photos are not oriented, because the thin sections were made from the pieces remaining after the test specimens had been prepared. As the four oriented photos (indicated by white horizontal arrows in Fig. 2) illustrate, sedimentary and deformation features such as bedding and foliation typically are oriented at a large angle to the core axis. Since the SAFOD core is not oriented we do not have information on how these cores are rotated along their axis relative to vertical; thus we cannot definitively relate the orientation of textures in the rocks to that of the fault. With the major exception of the SDZ and CDZ, mineral-lined fractures cross-cut fabric elements in all of the core samples examined in this study (see also Holdsworth et al., 2011).

Textures and mineral assemblages of the CDZ and SDZ are nearly identical, consisting of porphyroclasts of serpentinite and other, largely sedimentary, rock types dispersed in a well foliated (e.g., Sills et al., 2009; Sills, 2010; Chester et al., 2010), soft and friable matrix of Mg-rich, saponitic and corrensitic clays (Moore and Rymer, 2012). The samples readily separate along the foliation planes (Fig. 2). These clay-rich gouges are very weak, with coefficient of friction, $\mu \approx 0.15$, in marked contrast to the frictional

strengths of the Great Valley Group rocks on either side of the CDZ, with an average $\mu \approx 0.45$ (Carpenter et al., 2011, 2012; Lockner et al., 2011). The Great Valley rocks consist largely of shales and siltstones, with some sandy layers. The sedimentary units close to the SDZ are considerably more deformed overall than those near the CDZ (Fig. 2); Holdsworth et al. (2011) refer to these different sections as “inactive fault rocks” (that is, not currently creeping) and “relatively undeformed host rocks”, respectively.

3. Measurement procedure

3.1. Intact samples: permeability as a function of pressure

The primary set of permeability measurements was carried out under hydrostatic conditions on intact core samples at controlled confining pressure and pore pressure. The long adjustment time of many of these samples to changes in confining pressure as well as their low permeability meant that individual permeability determinations typically spanned one or more days. Test specimens were prepared from the core samples in different configurations, necessitated by the sample properties, to meet the requirement that the permeability measurements reflect flow parallel to the core axis. The most competent samples were prepared as cubes or prisms with nominal cross-section dimensions perpendicular to flow direction of 1.9 by 1.9 cm. In some cases, cubes could not be obtained and samples were fashioned into thin wafers with 1.9 by 1.9 cm faces and flow-parallel thickness ranging from 0.4 to 0.9 cm. If a sample was missing material, high-viscosity epoxy was added to the sides to fill out the deficient space and prevent fluid bypass. Top and bottom faces were left free of epoxy as much as possible to

Table 1
Permeability, porosity and density of intact SAFOD samples.

| Lithology | Measured depth, m | Core ^a | Range cm | k, m ² 40 MPa | k, m ² 100 MPa | γ^b 10 ⁻² MPa ⁻¹ | Porosity % | Density gm/cc | Uncertainty ^c % |
|--------------------------------|-------------------|-------------------|----------|--------------------------|---------------------------|---|------------|---------------|----------------------------|
| Foliated Siltstone-shale | 3188.48 | G-1-3 | 2–7 | 2.53e-21 | 6.92e-22 | 0.5 | 5.0 | 2.42 | 1.7 |
| | 3192.01 | G-2-2 | 19–22 | 2.94e-20 | 5.99e-22 | 4.1 | 1.9 | 2.48 | 1.5 |
| | 3192.56 | G-2-2 | 75–83 | 1.87e-20 | 3.41e-21 | 0.9 | 2.4 | 2.55 | 1.0 |
| Cataclasite | 3194.76 | G-2-5 | 25–30 | 2.85e-20 | 9.28e-22 | 3.5 | 4.4 | 2.25 | 1.0 |
| | 3195.52 | G-2-6 | 7–15 | 5.13e-19 | 1.70e-20 | 4.1 | | 2.66 | 0.7 |
| | 3196.07 | G-2-6 | 61–72 | 8.66e-21 | 2.97e-22 | 3.8 | | 2.12 | 4.0 |
| | 3196.28 | G-2-7 | 0–5 | 2.07e-20 | 1.10e-20 | 0.6 | 5.7 | 2.35 | 1.0 |
| Clay gouge (SDZ) | 3197.71 | G-2-8 | 50–55 | 1.28e-21 | 4.83e-22 | 0.0 | | | |
| | 3197.71 | G-2-8 | 50–55 | | 1.75e-22 | | | | |
| Siltstone with Carbonate vein. | 3198.63 | G-3-1 | 22–27 | 4.39e-18 | 5.40e-19 | 2.1 | 3.9 | 2.67 | 0.8 |
| Banded Siltstone | 3198.84 | G-3-1 | 44–46 | 1.97e-19 | 1.81e-20 | 2.6 | 4.8 | 2.51 | 0.8 |
| | 3295.25 | G-4-1 | 34–37 | 7.74e-22 | 2.15e-22 | 1.1 | 8.7 | 2.32 | 1.1 |
| | 3295.52 | G-4-1 | 61–67 | 8.74e-21 | 1.36e-21 | 3.1 | 4.6 | 2.51 | 1.1 |
| | 3295.52 | G-4-1 | 61–67 | 1.34e-20 | 7.42e-21 | 0.9 | | | |
| | 3295.83 | G-4-2 | 2–5 | 1.04e-21 | 1.65e-22 | 1.5 | 7.1 | 2.39 | 0.6 |
| Clay gouge (CDZ) | 3298.63 | G-4-5 | 14–20 | 5.21e-22 | 6.17e-23 | 3.6 | | | |
| | 3298.63 | G-4-5 | 14–20 | | 5.07e-22 ^d | | | | |
| | 3298.63 | G-4-5 | 14–20 | 5.92e-22 | | | | | |
| Foliated Siltstone-shale | 3300.13 | G-4-7 | 22–25 | 1.31e-19 | 2.70e-21 | 4.5 | | 2.33 | 2.8 |
| Massive Greywacke | 3301.74 | G-5-2 | 45–48 | 1.63e-20 | 2.88e-21 | 2.6 | 5.0 | 2.46 | 0.7 |
| | 3301.74 | G-5-2 | 45–48 | 1.16e-19 | 3.88e-20 | 1.3 | | | |
| Foliated Siltstone-shale | 3309.27 | G-6-3 | 8–12 | 2.93e-18 | 4.68e-20 | 4.5 | | | |
| | 3309.27 | G-6-3 | 8–12 | 2.26e-18 | 8.00e-19 | 2.3 | 7.0 | 2.34 | 1.2 |

^a Sample identification in core boxes. For example, first sample is from Hole G, Run 1, Section 3, depth range 2 to 7 cm from top of core section.

^b Value at the highest effective pressure measured, where γ becomes nearly constant.

^c Uncertainty values apply to both porosity and density.

^d Continuation of previous experiment, deformed to 10% shortening at 100 MPa.

minimize disruption of pore fluid flow. The surfaces of the samples were then lapped to a smooth finish, and cross-sectional area, minus any portion backfilled with epoxy, was estimated.

Porous Berea sandstone wafers (1.9 × 1.9 × 0.65 cm) were placed on the top and bottom of the test samples to provide a uniform pore pressure on the sample faces and simple, one-dimensional pore fluid flow. Berea sandstone has permeability around 10⁻¹⁵ m², many orders of magnitude higher than that of the SAFOD samples, and therefore can be neglected in our calculations of permeability from measured flow rates using Darcy's Law. The sample assembly was placed in a latex jacket to isolate the sample from the confining fluid, and then secured to steel endplugs that contained a pore fluid inlet and outlet and were machined with grooves to promote uniform fluid access to the ends of the samples.

Permeability was determined at progressively increasing effective confining pressures of 10, 20, 40, 70, 100, and 120 MPa in a pressure vessel at 23 ± 0.2 °C. Effective confining pressure is defined as $P_e = P_c - P_p$, where P_c and P_p are confining and pore pressures, respectively. To begin, the sample column was evacuated to ensure that no air remained trapped in the sample or tubing. Confining pressure was applied, and then pore fluid introduced to the sample. A servo-controlled pressure generator supplied constant pore pressure of 1–5 MPa to one end of the sample; the other end was vented to the atmosphere through fluid-filled pore lines, so that no evaporation could take place at the sample face. The volume change in the pressure generator has a precision of 10⁻⁵ cc and provides a direct measure of fluid flowing through the sample at constant upstream P_p . Because of the long time needed for steady-state flow to be established, pore fluid was forced through the sample for hours to days at each pressure step. In all tests the pore fluid was a brine solution designed to be equivalent to formation fluid in the SAFOD borehole. The solution constituents, in g/l, were: Cl⁻, 13.32; Na⁺, 5.34; Ca²⁺, 2.77; and K⁺, 0.22 (Lockner et al., 2011). While testing samples with the *in situ* or reconstituted brine is desirable,

implementation is not straightforward. Samples have partially dried during storage and preparation, leaving excess salts in the pore space. Re-saturation with distilled water should bring the samples back to near starting salinity, but then continued permeability tests with distilled water would systematically reduce brine content. Since the swelling clays in the SAFOD samples tend to become unstable in low salinity fluid, we reasoned that too high salinity would be better than too low. The most permeable samples were initially flushed with multiple pore volumes of brine. However, for the majority of samples permeability was too low to make a complete exchange of pore fluid practical.

Permeability, k , was calculated at each effective pressure according to Darcy's law

$$k = \nu \left(\frac{l}{A} \right) \left(\frac{Q}{\Delta P_p} \right), \quad (1)$$

where Q is volumetric flow rate, l and A are length and cross-sectional area of the sample, ν is the dynamic viscosity of the pore fluid (0.95 centipoise in this case, or 9.5×10^{-4} Pa-s in SI units), and ΔP_p is the pore pressure drop across the sample. Accuracy of the measurements varied with permeability and was approximately ±5% for values above 10⁻²⁰ m² and ±10% for values between 10⁻²⁰ and 10⁻²³ m². The two largest sources of error were the daily room temperature changes (affecting flow rate measurement) and time-dependent relaxation of the samples that could last from hours to days. An example of these effects is shown in Appendix 2. The practical lower limit of permeability determination in our test system is the leakage rate in the pore pressure generator and volumometer. An 18 day leak test of the pressurized system without a sample yielded a flow rate of $(1.9 \pm 2.6) \times 10^{-10}$ cm³/s. For a typical sample, this flow rate would represent $k \sim 2 \times 10^{-24}$ m², 30 times less than our lowest measured value.

Pore pressure, effective pressure and permeability all vary across the sample during a permeability test. We report permeability based on average pore pressure, $P_0 = (P_{\text{high}} - P_{\text{low}})/2$ (where P_{low} is atmospheric pressure) and the corresponding effective pressure $P_e = P_c - P_0$. Since k depends on effective pressure (Section 4.1), this procedure leads to a bias in calculated permeability, but as shown in Appendix 3, it is no more than 0.2%. Another important issue in interpreting the laboratory-derived permeability values is how sample disturbance due to core retrieval and sample preparation

affects the measurements. We addressed this issue by performing repeated stress cycles on selected samples and observing the effect of stress history on permeability. These tests are discussed in Section 4.1 and in Appendix 3.

3.2. Intact foliated gouge: permeability during deformation

Of prime interest is determining how permeability of the foliated gouges in the CDZ and SDZ are affected by deformation, since repeat measurements of casing deformation show that these gouge zones are creeping (Zoback et al., 2010). We determined variations in gouge permeability with deformation in two ways: 1) by measuring permeability during axial shortening tests on intact samples, wherein fluid flow direction is parallel to the shortening direction, and 2) by measuring permeability across disaggregated and reformed gouge layers sheared between sandstone forcing blocks separated by an inclined sawcut. For the first type of experiment, intact samples of foliated gouge were carefully cut into cubes approximately 1.9 cm on a side. The samples were jacketed and pressurized in a manner similar to the samples described above. For these gouge samples, the chosen P_e was limited to 100 MPa, so that the permeability during deformation would not be too low to measure. The gouges were deformed at an axial shortening rate of $1 \mu\text{m/s}$ to 10% shortening (around 2 mm, depending on sample length), while axial load, σ_1 , and displacement were

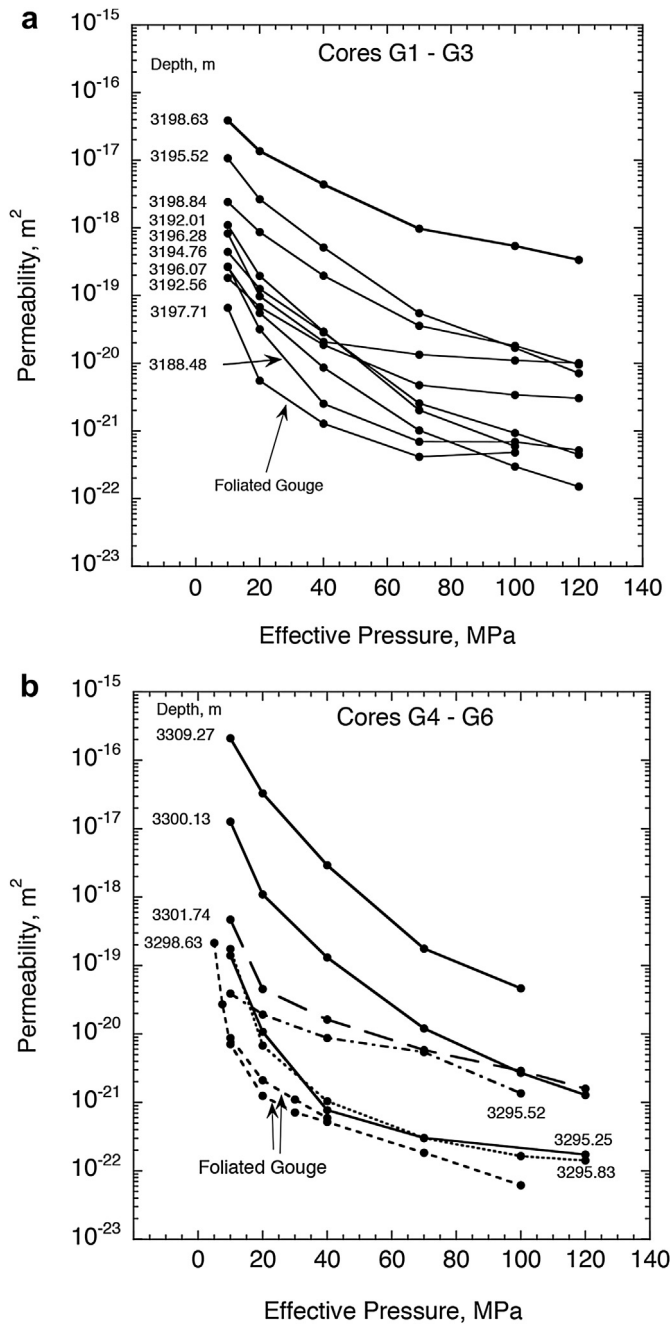


Fig. 3. Permeability as a function of effective confining pressure for intact SAFOD samples from a) cores G1–G3, adjacent to and including the SDZ and b) cores G4–G6, adjacent to and including the CDZ. The foliated gouges (3197.71 and 3298.63 m) had the lowest values. Permeability measurements progressed from low to high effective pressures.

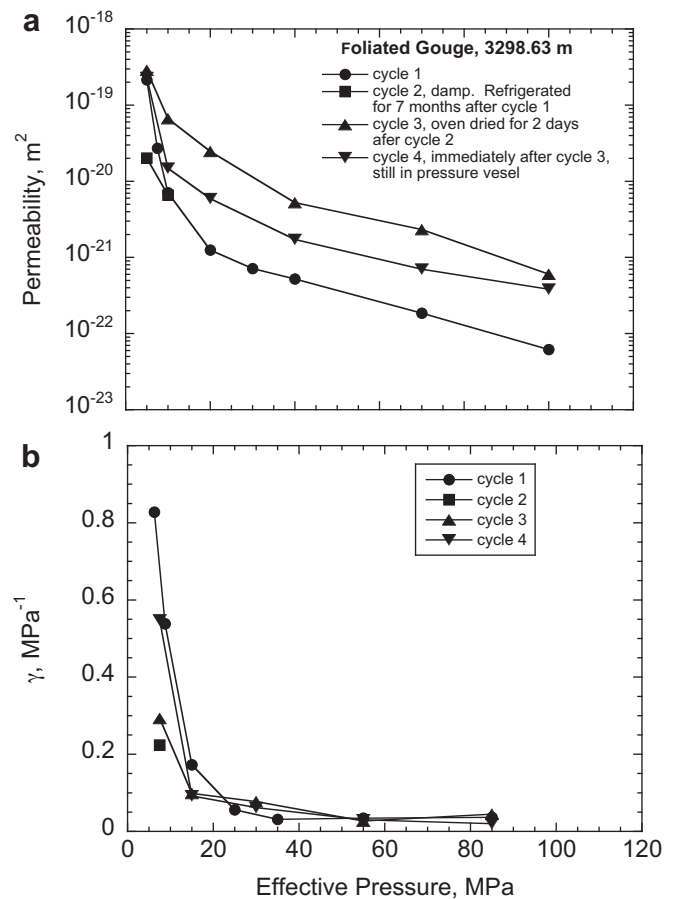


Fig. 4. Effective confining pressure cycling of an intact foliated gouge sample from 3298.63 m. a) Permeability. b) Effective confining pressure sensitivity of permeability (eq. (3)). In each cycle, permeability measurements progressed from low to high effective pressures.

recorded along with the pore and confining pressure data. (The triaxial test geometry is axi-symmetric, so during deformation tests, $\sigma_2 = \sigma_3 = P_c$.) Axial shortening was stopped periodically to measure permeability, as described above. These pauses generally lasted one to two days in order for steady-state flow through the sample to be established (see, for example, Appendix 2). Permeability data were corrected for the changing length and cross-sectional area during axial shortening, assuming a Poisson ratio of 0.33.

3.3. Disaggregated foliated gouge: permeability during shearing

Because the gouges are difficult to cut, we were unable to prepare intact samples from all of the SDZ and CDZ material available to us. For this reason, we also conducted simultaneous shearing and permeability tests on disaggregated gouge. If intact and disaggregated samples of the same gouge behaved in a similar manner during shearing, we felt confident that the disaggregated sample results for gouges where intact samples were not available would be relevant. In addition, disaggregated gouges can be sheared to a much larger strain than the intact samples.

Samples of CDZ (3296.86 and 3297.72 m) and SDZ (3197.56 and 3197.71 m) foliated gouge were crushed and passed through a 150 micron sieve. Mixed with simulated formation brine to form a paste, 2-mm-thick gouge layers were applied to artificial fault surfaces cut at 30° to sample axes in Berea sandstone driving blocks. Test samples were placed in a latex jacket and sheared at constant effective normal stress, $\bar{\sigma}_n = 120$ MPa, similar to the estimated $\bar{\sigma}_n$ in the borehole (assuming hydrostatic P_p) (Lockner et al., 2011). Pore pressure was fixed at 1 MPa at the inlet of the sample, and vented to atmospheric pressure at the outlet, resulting in fluid flow normal to the sawcut fault plane. Samples were sheared at a fault-parallel rate of 2.31 $\mu\text{m/s}$. Shearing was stopped at axial shortening of 0, 3, 6, and 9 mm for periods of 4–14 hours while steady-state permeability measurements were made. While flow measurements can be made during deformation, the low sample permeability would make it uncertain that a constant pore pressure gradient was maintained within the gouge layer. To assure

accurate permeability determinations, we chose to cease deformation and assure that steady flow conditions were established. The strength–displacement data were corrected for jacket strength, seal friction, and true contact area (see, for example Tembe et al., 2010; Lockner et al., 2011). Permeability was calculated from eq. (1) using the true contact area during sliding and the thickness of the gouge measured after sample removal. While gouge compaction was not measured during the tests, most of the decrease in thickness is assumed to occur during the application of normal stress. By 9 mm of axial shortening, the corrections for decreased contact area and sample thinning approximately cancel each other in the l/A ratio in eq. (1), and uncertainties in these corrections thus have little effect on the determined permeability.

4. Results

4.1. Permeability as a function of effective pressure

The permeability of intact core samples from Hole G, surrounding and including the SDZ and CDZ, decreased by 2–4 orders of magnitude as effective confining pressure increased to 120 MPa (Fig. 3). Overall permeabilities range from 10^{-16} to 10^{-23} m^2 , dropping most rapidly at the lower effective pressures. Two of the most permeable samples, the siltstones at a measured depth of 3198.63 and 3309.27 m (Fig. 3a and b) contained through-going fractures that were visible even before the samples were tested. These fractures likely dominated fluid flow. However, in most tests, no through-going fractures were observed, in which case fluid flow was assumed to be distributed throughout the entire sample and reported values represent matrix permeability. The foliated gouges at 3197.71 m (SDZ) and 3298.63 m (CDZ) measured depth generally had the lowest permeability at each pressure, probably due to the fine grain size and clay-rich mineralogy of the material. Notice the close agreement of two separate samples from 3298.63 m in Fig. 3b at $P_e = 10$ –40 MPa.

The decrease of permeability with effective stress is often described according to the relation

$$k = k_0 \exp(-\gamma(\bar{\sigma} - \bar{\sigma}_0)), \quad (2)$$

where $\bar{\sigma}$ is the effective mean stress $\bar{\sigma} = (\sigma_1 + \sigma_2 + \sigma_3)/3 - P_p$, k_0 is the permeability at reference stress state $\bar{\sigma}_0$, and γ is pressure sensitivity. $\bar{\sigma}$ reduces to P_e for hydrostatic loading (see, for instance, Wong and Zhu, 1999; Rice, 1992). In eq. (2), γ is independent of pressure. If pressure sensitivity of permeability varies with effective stress as shown in Fig. 3, then variations in pressure sensitivity with effective stress can be approximated by

$$\gamma(\bar{\sigma}) = \frac{\Delta \ln k}{\Delta \bar{\sigma}}. \quad (3)$$

Pressure sensitivity of permeability can depend on many factors, such as whether the material has been stress cycled (Wibberley and Shimamoto, 2003), or how long the sample is allowed to relax between cycles. The samples in Fig. 3 have all undergone the same stress and temperature history after acquisition; cores were brought to the earth's surface where they decompressed and cooled, sat for an extended period of time in the SAFOD core repository, partially dried when hermetically sealed core boxes were periodically opened for sampling, and then repressurized in the laboratory tests. The strong pressure sensitivity of permeability at lower P_e is most likely to be an artifact of damage induced by this sampling history (Morrow and Lockner, 1997). Thus in Table 1 we list γ at the highest pressures tested (i.e., where pressure sensitivity becomes nearly constant) as the most representative *in situ* value.

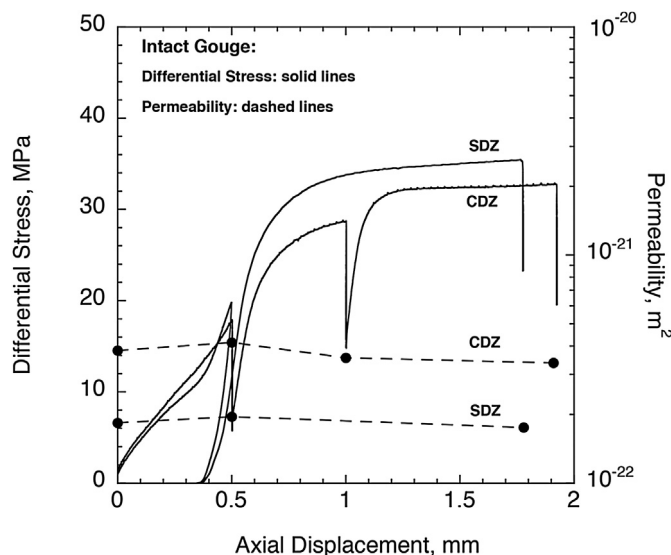


Fig. 5. Differential stress (solid lines) and permeability (dashed lines) during axial shortening for two intact foliated gouge samples from 3197.71 m (SDZ), and 3298.63 m (CDZ) at $P_e = 100$ MPa. Pauses in axial shortening during permeability measurements resulted in recoverable differential stress drops.

These values are similar to values compiled by Wong and Zhu (1999).

Selected samples were pressure-cycled multiple times including after treatments to vary sample moisture content to determine how permeability recovery depended on unloading time and sample desiccation state. We show an example of a friable foliated gouge from 3298.63 m MD that was pressure cycled four times (Fig. 4). Other examples, an intact cataclasite (3196.28 m), a massive graywacke (3301.74 m), and a fracture-dominated siltstone-shale (3309.27 m) underwent different cycling histories and are shown in Appendix 3. Cycle 1 of the foliated gouge sample (Fig. 4a) was characterized by a rapid decrease in permeability at low effective pressure followed by a gradual decline to a value below 10^{-22} m². The sample was then refrigerated for seven months while remaining in a damp state in a sealed container. Following this rest period, the sample was re-tested. This second stress cycle showed partial recovery of the initial permeability value. The sample was then evacuated and dried for two days at 60 °C. Cycle 3 showed full recovery of the initial value and much higher overall permeability values. Upon cycling a fourth time without removal from the pressure vessel and held at 5 MPa P_e , permeability was lower than that measured during the third cycle, but was permanently offset above the initial (cycle 1) values. These trends can be compared by plotting pressure sensitivity γ versus effective confining pressure (Fig. 4b). Initial (low effective pressure) γ values vary greatly among the individual cycles, depending on duration of preceding recovery and on sample moisture content, whereas the values at higher pressure are fairly consistent among the cycles. These pressure-cycling tests demonstrate that the reported permeabilities of the samples, such as those in Fig. 3, depend on the effective stress history, including the time-dependent poroelastic response to stress changes and changes in sample desiccation. This subject is discussed in more detail below.

4.2. Strength and permeability of gouges during deformation

Differential stress ($\sigma_1 - P_c$, solid lines) and permeability (dashed lines) are shown in Fig. 5 for intact samples from 3197.71 m (SDZ), and 3298.63 m (CDZ) deformed to 10% axial shortening at a constant P_e of 100 MPa. By 10% axial shortening (1.8 mm axial displacement), the differential stress of the SDZ sample had reached 35.4 MPa, compared to a peak differential stress of 32.7 MPa for the CDZ sample. The greater strength of the SDZ sample is due in part to its higher concentrations of quartz and feldspar compared to the CDZ (Lockner et al., 2011). Permeability of both samples remained nearly unchanged as a result of axial deformation, at around 1.7×10^{-22} m² (SDZ) and 3.7×10^{-22} m² (CDZ). These results are consistent with findings of Morrow et al. (1984), who showed that while permeability typically decreases with shearing for many types of both clay-rich and non-clay gouges for permeabilities above around 5×10^{-22} m², permeability below this value remains essentially constant with shearing. The permeabilities obtained at 10% axial strain are in close agreement with the disaggregated gouge data described next.

Coefficient of friction ($\mu = \tau/\bar{\sigma}_n$) (solid lines) and permeability (dashed lines) at $\bar{\sigma}_n = 120$ MPa are shown in Fig. 6 as a function of axial displacement for the disaggregated foliated gouge samples from the SDZ (3197.56 and 3197.71 m) and CDZ (3296.86 and 3297.72 m) sheared between sandstone forcing blocks at $P_e = 120$ MPa. The total axial displacement of 9 mm corresponds to 10.4 mm of fault-parallel displacement (a shear strain of 5.2 for a 2 mm-thick sample). Pauses during shearing at 3 and 6 mm for permeability measurements caused the gouge to relax and frictional strength to drop, but strength recovered completely once shearing resumed. These SDZ and CDZ gouges were weak even in

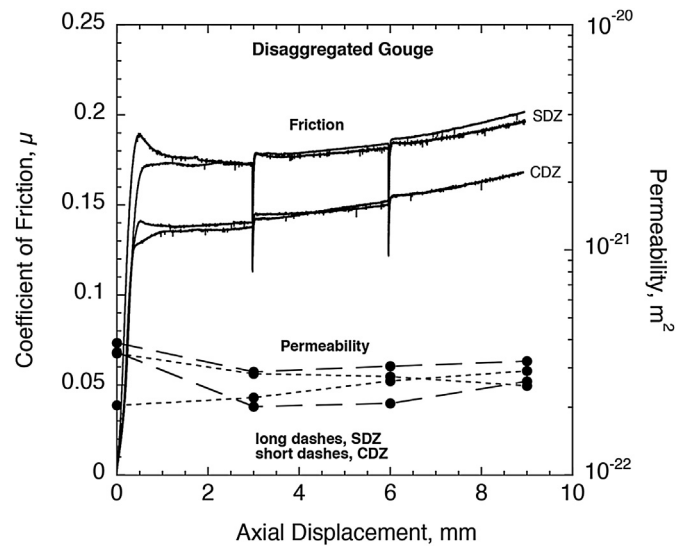


Fig. 6. Coefficient of friction (solid lines) and permeability (dashed lines) during shearing for disaggregated samples from the CDZ (3296.86 and 3297.72 m) and SDZ (3197.56 and 3197.71 m) at $\bar{\sigma}_n = 120$ MPa. Sliding was halted during the permeability measurements, resulting in a recoverable drop in frictional values due to sample relaxation. (1 mm axial displacement = 0.57 apparent shear strain for a 2 mm-thick sample, assuming no compaction).

disaggregated form because the smectite clay mineral saponite comprises roughly 60–65% of the volume fraction of the gouge matrix (Lockner et al., 2011). Strength values ($\mu = 0.14$ – 0.19) reported here are consistent with those reported by Lockner et al. (2011) for the same samples. Permeability of these foliated gouges, measured at 0, 3, 6 and 9 mm of axial displacement, was approximately 3×10^{-22} m² and was insensitive to shearing, indicating that most of the permeability loss occurred during the initial loading to 120 MPa effective normal stress, and that the initial permeability was low enough that shearing had little effect (see also Morrow et al., 1984).

4.3. Permeability profiles across SAF

Permeability profiles across the two core segments of Hole G are summarized in Fig. 7 and Table 1. Although observations during SAFOD drilling together with analysis of the ratio of P- and S-wave velocities from borehole logs do not indicate the presence of significantly overpressured fluids within the fault zone (Zoback et al., 2011), *in situ* pore pressure within the SAF has not yet been directly determined in SAFOD. Thus, it is not yet known what effective pressure is appropriate to use in interpreting the laboratory measurements presented here. Since our measurements (Fig. 3) show that the matrix permeability has strong pressure sensitivity, data for measurements at both 40 and 100 MPa effective confining pressure are shown in Fig. 7. Also shown are permeability values from intact foliated gouges deformed to 10% axial strain (downward triangles, see Fig. 5 and footnotes to Table 1), and disaggregated foliated gouges sheared to a strain of 5.2 (black upward triangles, see Fig. 6). As shown in Fig. 7, an effective confining pressure increase from 40 to 100 MPa reduces permeability by a factor of between 2 and 30 with an average decrease of about one decade. Permeabilities of rocks on either side of the deforming zones show a broad range of values from 10^{-18} to 10^{-23} m², whereas samples from the SDZ and CDZ, whether intact or sheared, are consistently at or below 10^{-21} m². As noted earlier, the samples

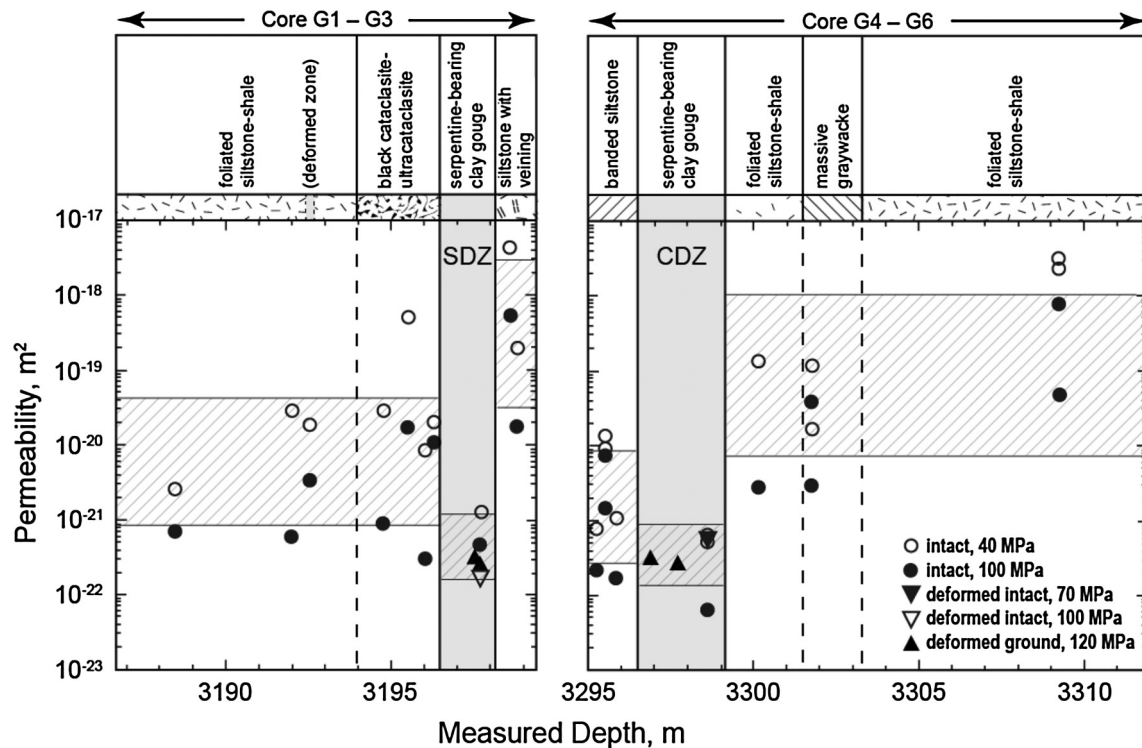


Fig. 7. Permeability of intact samples at 40 and 100 MPa (circles), and deformed ground core at 120 MPa (black upward triangles) as functions of measured depth in Hole G. In addition, permeability of intact core samples from 3197.71 m, deformed at 100 MPa (open downward triangle), and from 3298.63 m depth, deformed at 70 MPa (black downward triangle), are shown. Lithology from Bradbury et al. (2011). The deforming zones SDZ and CDZ are shown as vertical gray bands. Horizontal cross-hatched bands represent one standard deviation in the combined 40 and 100 MPa permeability data for each segment.

at 3198.63 and 3309.27 m with the highest measured permeability values contained fresh macroscopic fractures that were probably formed during core retrieval and/or sample preparation. These values represent upper bounds on the matrix permeability.

It was not possible to measure porosity of the foliated gouges of the CDZ and SDZ because of their friable nature. Porosity and density values obtained for samples from the other structural units (Table 1) show no consistent trends over the relatively narrow depth intervals we have studied. However, while there are a few exceptions, overall the sedimentary rocks from G1 to G3 have lower porosity and higher density than those from G4 to G6.

5. Discussion

5.1. Permeability structure of the San Andreas Fault and implications for fluid pressure

Given the large total shear offset on the San Andreas Fault, it is not surprising that a variety of lithological facies was encountered in the 30 m of core recovered from Hole G at SAFOD. Taken as a group, these fault-zone core samples show permeability ranging over 5 orders of magnitude with some foliated gouge samples, at effective pressure above 100 MPa, having permeabilities lower than our practical measurement limit. Wibberley and Shimamoto (2003) also reported a 5 orders of magnitude variation in permeability in a profile of surface samples taken from the Median Tectonic Line in southwest Japan, and they also found that permeability was low in fine-grained shear zones.

For the SAFOD core, we emphasize the general trend in permeability data in Fig. 7 by dividing the core into 6 groupings: two currently creeping fault segments represented by the SDZ and

CDZ (gray shading) and segments representing the rock units that flank these active deforming zones. Cross-hatched bands of permeability represent one standard deviation in the combined 40 and 100 MPa data for each segment. Borehole logging data (Zoback et al., 2010, 2011) indicated that the SDZ represents the southwest boundary of the present-day, ~200-m-wide SAF damage zone (Fig. 1b). Thus, the core from 3187 to 3196.4 m in Fig. 7 represents currently inactive, previously deformed fault material SW of the present SAF damage zone, while all other segments are from within the present damage zone (Bradbury et al., 2011; Holdsworth et al., 2011). Fig. 7 shows that there is little systematic difference in permeability between these previously deformed rocks SW of the present SAF damage zone and damage zone material between and to the NE of the clay-rich deforming zones.

As noted in Section 4, the foliated gouge has consistently low permeability. After initial compaction, permeability of the foliated gouge tends to be less pressure-sensitive than the surrounding rock. Therefore it is likely that the measured permeability ($<10^{-21}$ m²) is representative of the *in situ* gouge permeability at SAFOD between about 1 and 3 km depth. At temperatures above about 150 °C saponite should become unstable (Inoue and Utada, 1991). Thus, as discussed in Lockner et al. (2011), saponite is not likely to be found in the SAF near SAFOD at depths greater than 3.5–4 km. At these greater depths, other weak phyllosilicate minerals such as chlorite and talc are likely to replace saponite (and the related mineral corrensite) and are expected to also result in low fault core permeability (e.g., Sanford, 1982; Mori et al., 2007).

Our permeability measurements imply that the SDZ and CDZ will act as a cross-fault barrier to fluid flow, consistent with mud gas analyses carried out across the SAF at SAFOD (Wiersberg and Erzinger, 2008, 2011). They found that the proportions of

formation-derived H₂, CO₂ and CH₄ were different on the Pacific and North American plates, implying little or no cross-fault communication of these gases (i.e., that the SAF hydrologically separates the two plates). Low radon activity in the measured depth interval 3000–3500 m also indicates a low-permeability SAF because, due to its low mobility, radon migration is mostly controlled by active fluid flow (Wiersberg and Erzinger, 2008).

Although a few isolated repeating microearthquakes are occurring within the SAF nearby (Fig. 1a), most of the fault at this location – including where penetrated by SAFOD – is deforming by creep and is unlikely to exhibit significant time-dependent variation in permeability. Deformation tests on CDZ and SDZ gouge (Figs. 5 and 6) show that this material quickly attains a steady flow condition that shows little sensitivity of permeability to total shearing. Thus, pore pressure and permeability cycling, in which permeability creation during earthquakes (or other rapid slip) alternates with fault-zone mineralization (sealing) between earthquakes (Sibson, 1992; Sleep and Blanpied, 1992), seems unlikely to be an important process in the actively-deforming CDZ and SDZ at SAFOD.

Although veining is notably absent in cores from the SDZ and CDZ gouge (except in clasts), there is strong petrographic evidence for repeated fracturing and sealing episodes in core from the damage zone (Holdsworth et al., 2011). While the actively-deforming zones are continuously shearing (creeping) at their yield strengths, the surrounding damage zone material is notably stronger (Lockner et al., 2011; Carpenter et al., 2011, 2012). As suggested by Rice (1992), Chery et al. (2004), and Tembe et al. (2009), effective shear stresses in the plane of the SAF, which are limited by the strength of the foliated gouge, are below the yield limit of country and damage zone rocks. However, for the transpressional stress regime determined at SAFOD (Hickman and Zoback, 2004; Boness and Zoback, 2006), shear stresses on fractures oriented obliquely to the SAF can be significantly higher (i.e., reaching values predicted by Byerlee's Law), causing failure in the damage zone and adjacent country rock. Barton et al. (1997) showed that fluid flow along a major active normal fault in northern Nevada was dominated by critically stressed fractures, wherein, fractures that were not aligned with the current regional stress tended to seal and reduce permeability through precipitation reactions while the critically stressed, favorably oriented fractures remained open to fluid flow through continued deformation. If a similar process is occurring at SAFOD, then fluid flow in the damage zone (in contrast to the SDZ and CDZ) will be fracture dominated, which is consistent with the presence of through-going fracture-sealing textures in the damage zone and their absence in the SDZ and CDZ, as noted above. In this case, the appropriate *in situ* permeability in the damage zones may be 1–2 orders of magnitude higher than the matrix permeabilities reported here (Brace, 1980).

The extremely low permeability of the SDZ and CDZ would result in a slow time constant for equilibration of formation and borehole fluid pressures. This effect would mean that the *in situ* pore pressure within the deforming fault gouge would be difficult to determine from observations of borehole fluid influx during drilling and instead may require long-term pressure monitoring within the fault (Wang, 2011). Although long-term monitoring of pore pressure within the fault zone was an original part of the SAFOD science plan, such monitoring has yet to be realized owing to budgetary and operational difficulties. In the absence of such monitoring, controversy remains regarding fluid pressure in the SAF. Zoback et al. (2010, 2011) reported no definitive evidence for high or near-lithostatic fluid pressures within the SAF, based on borehole observations during and after drilling. The density of the drilling mud required to stabilize the hole was about 40% above

hydrostatic while drilling across the fault zone, which is considerably less than the pore fluid pressures that would be expected based on the high-pore pressure Rice (1992) model, yet no anomalous formation fluid influxes were observed during drilling. Furthermore, they noted that the ratio of P- to S-wave velocities measured with geophysical logging tools was relatively uniform across the damage zone and the SDZ and CDZ contained within it, which would not be true if abnormally high-pore fluid pressures were present. Wiersberg and Erzinger (2011) argue that the observed trip gas concentrations (gas samples taken during down time when the drill bit is being changed), also used to evaluate relative fluid pressures in the borehole and surrounding rock, are more indicative of wall rock permeability than high-pore pressure. However, since fluid influxes are a function both of excess fluid pressures (relative to drilling mud) and the permeability of surrounding formations, it is difficult to separate these two effects. In summary, although most of the available information still favors the idea that the actively-deforming SAF where crossed by SAFOD is not highly overpressured, the existence of high fluid pressures limited to the ultra-low-permeability SDZ and CDZ cannot be precluded.

Analysis of SAFOD core specimens by petrographic and TEM techniques has been used to suggest that high pressure might exist within the SAF. Holdsworth et al. (2011) argue that high-pore fluid pressure must have been present in the SAFOD core samples in order to explain how nanoscale porosity can persist in the cataclases. Janssen et al. (2010) also argue for high fluid pressures in order to explain stress-induced solution-precipitation features. However, it is well known that rocks can exhibit grain-scale microcrack (or other) porosity even under high effective confining pressures, due to the presence of grain-scale stress heterogeneities. Thus, the relevance of these types of microstructural observations to the issue of whether or not the SAF where penetrated by SAFOD is overpressured or not is unclear.

In his model of pore fluid pressure and its possible control on the low absolute strength of the SAF, Rice (1992) invoked the pressure dependence γ of permeability in the deforming fault core. In this model Rice proposed a leaky SAF in which a deep source fed pore fluid into the base of the fault system wherein the core of the fault is assumed to be more permeable than the adjacent rocks. Then, pore fluid pressure would rise as needed in the core of the fault to allow flow toward the surface, which was accompanied by leakage of fluid into the adjacent country rock. Given the low permeability of the fault material at high effective pressure assumed in his model, only a small portion of the deep-source water would escape into the surrounding rock at any given depth as it moved up the fault. In this way, a large lateral pore pressure gradient would develop in the fault core that would sustain high interior pore pressure and develop a zone of localized low shear strength.

The observations of fault structure and material properties that SAFOD has provided allow us to re-examine the Rice (1992) model, at least for this creeping portion of the fault and at the depths sampled by SAFOD. At a depth of 2.7 km, the current damage zone of the SAF is about 200 m wide. However, the active deforming zones SDZ and CDZ are 1.6 and 2.6 m wide, respectively, with a third possible deforming zone at the NE boundary of the damage zone (the NBF), as described in the Introduction. Such narrow deforming zones, separated by higher permeability material, probably cannot sustain the combination of high internal pore pressure, steady vertical fluid flow and low rates of lateral fluid flow required by the Rice model. Also, in the absence of a deforming fault core that is more permeable than the adjacent units (as assumed by Rice, 1992), Faulkner and Rutter (2001) show that permeability anisotropy within the fault zone must exceed 3

orders of magnitude for localized overpressures to develop as predicted by a Rice-type model, a scenario not supported by the negligible permeability anisotropy measured by Rathbun et al. (2012) on SAFOD gouges from the SDZ and CDZ. Also, the source of the fluid must be considered. Fulton et al. (2009) analyze the long-standing hypothesis that fluids released by dehydration reactions due to regional metamorphism may generate elevated fluid pressures that are localized within the SAF zone. They show that such a source is too small and short-lived to generate or sustain the elevated fluid pressures required to reduce the effective normal stress on the SAF enough to result in the low shear strengths required by heat-flow and stress measurements near the fault. Also, while direct measurement of *in situ* pore pressure within the SAF has so far proven to be problematic at SAFOD, the weak clay-dominated fault has intrinsically low frictional strength (Lockner et al., 2011; Carpenter et al., 2011, 2012) and is sufficiently weak, without the need to invoke high-pore pressure, to account for observations of low shear strength of the shallow fault. Deeper in the fault zone, the fault structure may differ and high fluid pressure, perhaps sustained by vertical flow of pore fluid, cannot be ruled out.

5.2. Extrapolation of permeability measurements to *in situ* conditions

Measured permeability in Fig. 3 spans 6 orders of magnitude with much of the variation due to effective pressure dependence. An important question to address is how the laboratory measurements of core permeability are related to *in situ* permeability. For example, if fault-zone pore pressure is elevated, would the permeability measured at low effective pressure be representative of *in situ* permeability, or is core recovery from depth and desiccation due to periodic sub-sampling of the core responsible for the measured values? Selected samples were pressure cycled to determine the memory of permeability to effective confining pressure history. We found that unloading samples from the peak P_e to the initial test pressure of 10 MPa while still in the pressure vessel resulted in minimal permeability recovery, even when samples were left in the test machine for many days (see Appendix 3). This minimal permeability recovery exhibited stress sensitivity γ that was typically consistent with the high- P_e limiting stress sensitivity listed in Table 1. Re-pressurizing the samples from this starting condition generally resulted in reduced permeability with this same low range of γ . Samples that were removed from the pressure vessel and allowed to sit at room pressure in sealed containers (without drying) for days to weeks showed significant permeability recovery. Samples that were allowed to dry showed greater, and in some cases full, recovery of starting permeability. These general trends were observed for both damage zone samples and foliated gouge from the SDZ and CDZ. The nearly complete permeability recovery that occurred in samples that were partially or fully dried suggests that the rapid drop in permeability exhibited by all samples during initial loading between zero and 20 MPa is in large part an artifact of core recovery and handling prior to sample testing and is probably significantly higher than corresponding *in situ* permeability values.

In a related point, the permeability measurements reported here, especially at higher confining pressure, typically required one–three days each. This is mainly due to the slow, time-dependent compaction of the clay-rich samples (see Appendix 2). Alternate testing techniques that use argon or nitrogen gas as a pore fluid can be accomplished in significantly shorter time. However, clay-rich samples (and especially samples with swelling clays such as the SAFOD core) have notably different

strength and other properties when pore water is present (Moore and Lockner, 2004, 2007; Morrow et al., 2000). Therefore, the response of pore structure as well as permeability to changes in confining pressure will be different in dry and saturated samples. An important consequence is that gas permeability measurements can be significantly different from water-saturated permeability measurements. Faulkner and Rutter, 2001, and Behnsen and Faulkner, 2011, explore this topic further, showing that the difference in water-argon permeability can be greater than an order of magnitude due to the hydrophobicity and hydrogen-bonding surface properties of the minerals tested.

While the *in situ* pore pressure and therefore effective mean stress within the deforming zones remain uncertain, our measurements indicate that permeability of SAFOD foliated gouge from the SDZ and CDZ at likely *in situ* P_e is very low (10^{-21} – 10^{-22} m²). This low permeability was measured for intact samples loaded hydrostatically, intact samples deformed to 10% axial shortening and disaggregated gouge deformed to over 500% shear strain. Intact sample permeability was measured in the direction parallel to the core axis (i.e., near fault normal), and permeability of sheared gouge samples was measured perpendicular to the sawcut fault planes. Computed Tomography (CT) core scans (Sills et al., 2009; Sills, 2010; Chester et al., 2010) show distinct alignment of clasts in the foliated gouge, parallel to the interpreted shear direction within the SAF suggesting that fault-parallel permeability might be higher than permeability measured parallel to the core axis, which is at high angles to the SAF. Although measurements of permeability anisotropy on highly sheared simulated gouge samples in experiments comparable to ours showed directional differences of about a factor of ten (Zhang et al., 1999), measurements of anisotropy on SAFOD CDZ gouge samples (Rathbun et al., 2012) showed negligible permeability anisotropy. Thus, it is likely that fault-parallel permeability of the actively-deforming gouge (not measured in this study because of limited sample availability) is similar to the permeability reported here.

While *in situ* permeability of the damage zone material and adjacent country rock is probably fracture dominated, as noted above through-going fractures are unlikely in the weak foliated gouge, which is highly plastic and massive. Therefore, the laboratory-derived matrix permeability measurements presented here should be appropriate for representing *in situ* values for the weak foliated gouge, but are probably lower bounds for the damage zone. The close agreement between roughly fault-normal intact gouge and disaggregated and sheared gouge permeability (Fig. 7) suggests that for CDZ and SDZ material, testing of disaggregated gouge, for which sample preparation is significantly easier, provides useful permeability data.

Wireline log velocity and resistivity as well as core analysis indicate that the SDZ represents the southwest boundary of the current SAF damage zone (Zoback et al., 2010, 2011). There is a suggestion of increasing permeability as the SDZ is approached from the southwest in the adjacent siltstone-shale and cataclastic rocks (3187–3196.5 m, Fig. 7). Such a trend might indicate an increase in microcrack damage within 5–10 m of the ~200-m-wide damage zone. However, denser sampling of permeability and associated petrographic analysis are required to confirm this suggestion. Permeability of damage zone rock to the northeast of the SDZ (3198.3–3199.6 m) was 2–4 orders of magnitude higher than the SDZ foliated gouge. In contrast to the SDZ, the CDZ was located near the center of the SAF damage zone (Fig. 1b). Permeability of damage zone rock surrounding the CDZ was generally higher than for the foliated gouge, but less so for rock SW of the CDZ than NE of CDZ, where values were less than 10^{-20} and

10^{-18} m², respectively (Fig. 7). At SAFOD as well as other fault zones, damage zone samples have pervasive fracture networks, and it is likely that fluid flow in the damage zone is fracture dominated. Episodic vein filling is also common in the damage zone samples (Holdsworth et al., 2011, and Appendix), and (with the exception of some veins that might predate the current faulting environment), this suggests that permeability within the damage zone may vary significantly over the earthquake cycle. Our permeability measurements across the SAF (Fig. 7) are consistent with the results of Wibberley and Shimamoto (2003), who found that structural complexities caused permeability differences of 5 orders of magnitude across the Median Tectonic Line in southwest Japan, with no apparent pattern, on either side of the central slip zone. Faulkner et al. (2003) found similar complexity for the Carboneras fault. Mature strike-slip faults with large total offsets can develop wide damage zones containing varied rock types and multiple slip surfaces. Repeated episodes of fracturing and healing are likely to create a heterogeneous fault core/damage zone complex. In contrast, Lockner et al. (2009) found that a much simpler symmetrical permeability/damage model was sufficient to represent the less structurally complex Nojima fault at Hirabayashi, Japan.

6. Conclusions

Our measurements showing low permeability of the SAFOD core samples, in agreement with other fault-zone studies, suggest that the actively-deforming fault segments of the San Andreas Fault will act as a barrier to fluid flow across the fault. These low permeabilities, taken in conjunction with mud gas analyses at SAFOD reported by Wiersberg and Erzinger (2008, 2011), suggest that models of fault behavior requiring high permeability and/or continuous fluid flux from the mantle are not consistent with the current experimental and field evidence, at least at the upper 3 km of the crust investigated by SAFOD drilling. The low matrix permeability of the actively-deforming zones ($<10^{-21}$ m²) as measured over a broad range of effective mean stress and shear strains is probably a good representation of the *in situ* permeability of the weak clay-rich gouge zones. Damage zone and adjacent fault rock matrix permeabilities are generally higher (10^{-18} – 10^{-21} m²). However, this probably represents a lower bound to the *in situ* permeability of these rocks, which likely contain pervasive fracture networks that, at least for portions of the earthquake cycle, should dominate fluid flow. Close agreement of permeability measured on intact gouge and disaggregated gouge samples implies that disaggregated CDZ and SDZ material can be used to infer *in situ* permeability. A complete understanding of the hydraulic properties of the San Andreas Fault at SAFOD will require further study and in particular, direct measurement of pore fluid pressure in the actively-deforming zones. However, the current observations of extremely low matrix permeability for deep core samples from the SAF provide new constraints on the hydrology of the fault system at SAFOD.

Acknowledgments

This manuscript was greatly improved by comments from E. Roeloffs, C. Neuzil, D. Saffer and an anonymous reviewer.

Appendix 1. Intact-rock sample descriptions

Because of the very close similarity of the CDZ and SDZ foliated gouges, the intact samples obtained from the two creeping strands are described together. The rock units from which the other intact samples (Table 1) are derived are described in sequence with

increasing measured depth in Hole G. Sample locations are shown in Fig. 2 relative to the lithologic/structural interpretations of Bradbury et al. (2011), along with photos illustrating representative features of each unit.

A set of these thin sections has been archived and is available for study (go to www.earthscope.org for information). Note that the thin sections of the 3301.74 and 3309.27 m MD samples were prepared from the run products of permeability experiments, and the sections include the wafers of Berea sandstone that were placed at the top and bottom of the samples (see text).

A1.1. Samples within SDZ and CDZ

A1.1.1. Serpentinite-bearing clayey gouge (3197.71 and 3298.63 m MD in Hole G)

The foliated gouges of the SDZ and CDZ consist of porphyroclasts of serpentinite and other, largely sedimentary rock types dispersed in a well foliated, soft and friable matrix of Mg-rich clays. Although neither of the thin sections was prepared from an oriented rock specimen, the photos in Fig. 2 were oriented consistent with the general observation that the foliation direction and preferred orientation of the porphyroclasts is perpendicular to the core axis (i.e., roughly fault-parallel). Locally, the foliation has a folded or contorted appearance, and slickensides in all orientations are present (see Phase 3 Core Atlas, at www.earthscope.org). Similarly, individual porphyroclasts were found with all orientations, including perpendicular to the general trend. The largest porphyroclasts observed in the thin sections are ~6 mm long and 2–3 mm wide.

Minor differences in texture and mineralogy between the CDZ and SDZ samples may be related to their different degrees of active slip. We estimate that the gouges consist of ~60–65% clays by volume, with the proportion being slightly higher in the CDZ than the SDZ. Correspondingly, the porphyroclast content of the CDZ is somewhat lower. In addition, while the CDZ sample showed no evidence of calcite deposits in the gouge matrix, consistent with the observations of Holdsworth et al. (2011), the SDZ sample (3197.7 m) contains a ~1.5 mm long deposit of clear, blocky calcite along a foliation surface. Other such calcite veinlets in the SDZ have been described by Moore and Rymer (2012).

A1.2. Samples external to SDZ: cores G1–G3

A1.2.1. Foliated siltstone-shale (3188.45, 3192.01, and 3192.56 m MD)

This rock unit is very quartz-rich and very fine-grained for the most part, although grains in the shallowest sample (3188.48 m) reach coarse sand size (maximum ~0.65 mm diameter compared to a maximum grain diameter of ~0.3 mm for the sample at 3192.01 m). Overall, the samples are a light brownish-red in plane-polarized light, but nearly colorless patches where the quartz-rich matrix has recrystallized give them a mottled look (especially at 3192.01 m). The rock unit has been brecciated and infilled with dark-brown, Fe-rich deposits (see also Fig. 2 of Holdsworth et al., 2011). The middle sample (3192.01 m) is highly veined by calcite ± anhydrite ± zeolites.

The deepest sample (3192.56 m) comes from a narrow fault that was identified by Bradbury et al. (2011) at ~3192.5 m. It is extremely fine-grained overall, with scattered porphyroclasts that are identical in appearance to the highly veined portions of the 3192.01 m sample. The fine-grained matrix shows a well-defined foliation that in places forms mm-scale folds. Boudinaged porphyroclasts help define the foliation, which is oriented at a large angle to the core axis (Fig. 2). This fabric is cut by narrow calcite-lined fractures. Although Bradbury et al. (2011) refer to this

deformed zone as a “clay gouge” (their Fig. 2), X-ray powder diffraction analysis shows that the 3192.56 m sample, as well as those at 3188.45 and 3192.01 m, has very high quartz and low phyllosilicate contents. In their characterization of the SAFOD core, Holdsworth et al. (2011) define a second structural unit in the depth interval ~3190.6–~3194 m that consists of a gray foliated gouge cut by a darker-gray gouge at the position of the deformed zone (Fig. 2). However, our 3192.01 m sample is identical with respect to both mineralogy and textural/structural features to the one at 3189.7 m shown in Fig. 2d of Holdsworth et al. (2011), suggesting that both are part of the same lithologic unit.

A1.2.2. Black cataclasite to ultracataclasite (3194.76, 3195.52, 3196.07, and 3196.28 m MD)

This rock unit is very fine-grained, dense, dark-colored, and quartz-rich. The nearly black color in hand specimen arises from finely disseminated black material. The phyllosilicate content increases toward the SDZ, and at least some of the phyllosilicates are recently formed, fracture-filling minerals. The four intact-rock samples examined from this unit have been brecciated and sheared to varying degrees. For example, a strongly foliated, 0.5–0.7-mm-wide shear in the sample at 3194.76 m cross-cuts other structures at roughly a 20° angle. The rock also contains brecciated areas similar to those in the foliated siltstone (e.g., 3192.01 m), although here the void spaces are filled with calcite ± zeolites (?) ± pyrite. Both the shear and the brecciated areas are cross-cut at large angles by calcite ± phyllosilicate (?) filled fractures. Minor patches of lighter-gray, recrystallized quartzose matrix resemble portions of the foliated siltstone–shale.

The sample at 3195.52 m is extremely fine-grained and a dull grayish-brown color overall, but it contains an irregular, reddish-colored band of quartz-rich clasts in a phyllosilicate-rich matrix. Single-crystal quartz clasts are all <0.1 mm diameter; polycrystalline-quartz clasts reach ~0.7 mm in length. The sample from 3196.07 is very similar to the one at 3195.52 m, as well as to one of two rock chips from 3196.28 m that were sectioned.

The sample from 3196.28 m, which is located only a few cm from the southwest boundary of the SDZ, is variably sheared across its width (orientation relative to the core axis is unknown). The foliation of the 5-mm-wide section at the edge of the sheared side is overprinted by anastomosing bands of a foliated, grayish-brown, phyllosilicate-rich gouge that somewhat resembles a highly indurated version of the SDZ. In contrast to the SDZ, however, the porphyroclast population consists almost exclusively of polycrystalline-quartz pieces, along with a small number of siltstone porphyroclasts. No serpentinite clasts were found in this sample. Narrow calcite-filled fractures cross-cut nearly all of the fabric elements at a large angle and are only slightly disrupted across the indurated, phyllosilicate-rich gouge.

A1.2.3. Siltstone with veining (3198.63 and 3198.84 m MD)

The two samples collected from this unit for study differ markedly from those on the other side of the SDZ. These are quartz and feldspar-rich (K-feldspar is abundant) and relatively phyllosilicate-poor siltstones to fine sandstones, which are heavily cemented with calcite and some anhydrite. A few narrow bands of sheared and possibly recrystallized quartz and feldspar is overprinted by narrow calcite veins and generally wider veins of anhydrite ± calcite. The sample situated slightly closer to the SDZ (3198.63 m) is coarser-grained, with clasts reaching ~0.7 mm in length (coarse sand size). It also has the widest veins (to ~1.5 mm) with significantly larger anhydrite

crystals (tabular crystals to ~1 mm long). In comparison, the sample from 3198.84 m has a maximum grain size of ~0.25 mm (fine sand size), and somewhat narrower veins (<1.2 mm wide) filled with relatively short (≤0.4 mm long) and stubby anhydrite.

Both of these samples correspond much more closely to the description of this unit as a “siltstone with veining”, as reported by Bradbury et al. (2011) than to the “gray foliated gouge” of Holdsworth et al. (2011). However, the samples examined by Holdsworth et al. (2011) were situated closer to the SDZ than those selected for this study, and their samples may reflect deformation localized along the contact with the SDZ.

A1.3. Samples external to CDZ: cores G4–G6

A1.3.1. Banded siltstone (3295.25, 3295.52, and 3295.83 m MD)

The banded siltstone immediately southwest of the CDZ shows well-defined but fine-scale layering, characterized by alternating shaly and silty horizons, that is oriented at a large angle to the core axis. Typically, detrital grains in these layers are ≤0.25 mm long, with a maximum grain size of ~0.5 mm. These well-bedded horizons alternate with ones that are more disrupted, consisting of chunks of the sediments randomly mixed in a very poorly sorted matrix. Some clasts of volcanic rock and detrital serpentinite (now thoroughly altered to Mg-Al-rich clays) in the disrupted zones can exceed 2 mm in length. Holdsworth et al. (2011) attribute the irregularities in bedding features to soft-sediment processes, including bioturbation, whereas Bradbury et al. (2011) consider these rocks to possibly represent tectonic mélange. Given the fact that the few oriented samples (relative to the core axis) from this rock unit that we have examined all show a similar overall bedding orientation, we favor the interpretation of Holdsworth et al. (2011). Calcite and anhydrite fill fractures and occur as patchy deposits in the sedimentary rocks.

Thin sections of the three banded siltstone samples were prepared from the rock chips remaining after sample preparation, whose orientations were not marked. The photograph of an oriented sample shown in Fig. 2 is from a piece of core that was collected immediately adjacent to the one at 3295.52 m for a separate petrographic study.

A1.3.2. Foliated siltstone–shale (3300.13 m MD)

This sample from the unit adjoining the CDZ on the northeast side is a relatively featureless, poorly sorted, reddish siltstone containing large patches of calcite (5–10 mm in longest dimension). There are also calcite-filled fractures in this sample, some of which show crack-seal texture and others a suggestion of pull-apart features. Most quartz and feldspar grains are ≤0.25 mm in diameter, generally angular and with low sphericity. A faint bedding is defined by a slight preferred orientation of detrital micas and elongate quartz and feldspar grains. The largest clasts are 1–2 mm-long, brownish-red fossil fragments.

A1.3.3. Massive graywacke (3301.74 m MD)

Overall, this is a relatively well-sorted, quartz-rich sandstone, but it contains some layers and patches of silty to shaly material. The shaly matrix is a dull brown color, and it is irregularly distributed across the sample. The degrees of roundness and sphericity of the detrital grains in this sample appear to be the highest of all the sedimentary rocks examined in this study. Quartzofeldspathic clasts are typically 0.1–0.2 mm diameter; the largest clast seen in the thin section is a mafic volcanic ~0.6 × 0.9 mm in size. Only minor amounts of calcite are present, mainly as pore-filling cement.

A1.3.4. Foliated siltstone-shale (3309.27 m MD)

This sample consists of alternating layers of siltstone, shale, and minor amounts of fine-grained sandstone, with the layers oriented at a large angle to the core axis. Quartz and abundant feldspar grains are subangular. This sample contains abundant reddish-brown, partly altered detrital biotite and apple-green chlorite, much of it of diagenetic origin (e.g., after biotite). Moderate amounts of calcite fill fractures and pore spaces; calcite veins are a maximum of ~ 0.25 mm wide. The wider calcite veins appear to offset sedimentary layers by as much as 0.7 mm. The tested sample contains numerous fresh fractures, which presumably formed during or after sample recovery.

Appendix 2. An example of time-dependent sample compaction

The time required to carry out these permeability tests was often dictated by the time-dependent relaxation of the samples following changes in effective pressure. An example of time-dependent compaction of an intact sample of foliated gouge during a permeability test is shown in Fig. A1. Fluid volume of brine flowing into or out of the high-pressure side of the sample is plotted as a function of time following an effective pressure increase from 70 to 100 MPa. Constant high- and low-side fluid pressures were maintained at, 4 MPa and atmospheric pressure, respectively. Following the effective pressure increase to 100 MPa, the sample compacts and water is steadily expelled as pore volume decreases. After about two days, the compaction rate has decreased to the point where a new steady fluid flow rate, Q , is established that is 54% of the steady-state flow rate observed at 70 MPa. This steady flow rate is used in eq. (1) to compute permeability, which dropped from 2×10^{-22} to 1.2×10^{-22} m². A subtle periodic peak in fluid volume appears at 1.6, 2.6 and 3.6 days (see boxed inset for an expanded view). This is the result of daily room temperature changes causing pore water in the sample/pore pressure system to expand.

The volume change indicated in Fig. A1 is the pore fluid expelled to the high-pressure side of the sample. By symmetry, we assume that (to a first approximation), an equal volume of pore fluid is expelled to the low pressure side, although this was not measured directly. (In this assumption, we recognize that the boundary conditions are not exactly the same at each end of the sample). Consequently, the loss in pore volume within the sample, ΔV , during this pressure step, is about twice the fluid volume expelled into the high-pressure side of the apparatus. Thus, $\Delta V \sim 0.09$ cc, or 1.2% of the initial sample volume. In this example, the pore volume transient is well fit by an exponential decay: $\Delta V \propto \exp(-t/t^*)$ with $t^* = 0.50$ days.

By recording the volume loss following steps in effective confining pressure, the cumulative porosity loss can be estimated. Log (cumulative volume loss) is plotted as a function of log(P_e) for 7 samples in Fig. A2. Each curve progresses from left to right with increasing effective pressure. Porosity loss for repeated pressure cycles is shown for two samples (triangular data points). Since the initial volume loss from zero pressure to the starting test pressure (generally $P_e = 10$ MPa) was not measured directly, it was estimated by back-projecting the volume-loss rate from the first recorded pressure step to zero pressure. A number of interesting features appear in Fig. A2. First, foliated gouge from both the CDZ and SDZ exhibit higher volume loss than country rocks and damage zone rocks, with the latter tending to group together. Second, all volume-loss curves exhibit power-law or near-power-law response to changes in effective confining pressure, with slopes between 0.5 and 1.0 for the foliated gouge and about 0.8–1.0 for the (stronger) country rock and damage zone samples. Third, there was significant

recovery in volumetric strain in the repeated samples during unloading between the first and second cycles. The second cycles showed less volumetric strain than the first but converged on approximately the same cumulative volumetric strain at the maximum value of P_e used.

Appendix 3. The effect of pressure cycling on permeability

Selected samples were pressure-cycled multiple times to determine how permeability recovery depended on unloading time and sample desiccation. We show examples of a black cataclasite (3196.28 m, Fig. A3), a massive graywacke (3301.74 m, Fig. A4), and a fracture-dominated siltstone-shale (3309.27 m, Fig. A5). The cataclasite (Fig. A3a) was pressure cycled once, and with the sample still in the pressure vessel, effective pressure was dropped to the starting value of 10 MPa for one day. Permeability was then measured during a second pressure cycle, after which the sample was removed from the pressure vessel. At this point, the sample was exposed to air and allowed to bench dry for 10 days before being re-saturated and pressure cycled a third time. During the first cycle, permeability decreased systematically to a value of around 10^{-20} m². Upon cycling a second time, there was almost no recovery in permeability: values remained fairly constant, and ended at permeabilities similar to those of the first cycle. This behavior is typical of low-permeability clay-rich gouges, as also seen, for example, by Morrow et al. (1984). When removed from the pressure vessel and later re-tested, permeability recovered to the initial values from cycle 1, and then showed a steep permeability decline as P_e was increased, attaining values about an order of magnitude lower than seen in the previous two cycles. These trends can be compared directly by plotting the changes in pressure coefficient γ (Fig. A3b) determined using eq. (3). Cycles 1 and 3 in this figure are more similar than cycle 2, because drying and time-dependent relaxation causes the sample to be more permeable even after re-saturation, whereas cycling immediately did not allow the permeability to recover to the high initial value. At the highest pressures, γ values were consistently around 0.01 MPa^{-1} or less, essentially insensitive to pressure.

The intact massive graywacke (3301.74 m, Fig. A4a) sat in a refrigerated container for five months after the first cycle, and was then oven dried before re-saturation prior to the second cycle. Because of the effects of long-term relaxation and drying, this sample recovered part (but not all) of the initial permeability. Values were near those of the first cycle but consistently lower, reaching a final permeability of around 10^{-21} m². Because the permeability curves were nearly parallel, pressure sensitivity (Fig. A4b) appeared similar for both cycles, and was fairly uniform at around $0.02\text{--}0.03 \text{ MPa}^{-1}$ at P_e of 40 MPa or greater. This range of γ is just high enough to be important for models of fault behavior that incorporate the pressure sensitivity of permeability, since permeability is still changing significantly with effective confining pressure, even at the higher effective pressures tested.

The sample from the siltstone-shale unit showed yet another variation on permeability behavior (Fig. A5a). This sample, which was cycled after a 3 hour recovery time at 10 MPa in the pressure vessel, showed very little permeability recovery upon unloading, just like the cataclasite (Fig. 3A). However, permeability continued to decrease during the second loading cycle, so that the final value was more than an order of magnitude lower than in cycle 1. Pressure sensitivity, γ , was nearly the same in both cycles at the higher effective confining pressures investigated ($0.01\text{--}0.03 \text{ MPa}^{-1}$, Fig. A5b), even though permeability was more than ten times lower. This permanent drop in permeability is likely the result of grain

crushing during closure of the macroscopic fractures in this sample, a non-elastic response.

To summarize, samples that are cycled immediately while still in the pressure vessel (i.e., remain saturated and pressurized) have a lower permeability at the beginning of the repeat cycle than the initial cycle, but tend to converge toward the same (or slightly lower) permeability at higher pressures. Fractured samples such as the foliated siltstone-shale (3309.27 m) also show little permeability recovery upon cycling, but continue to decrease during cycle 2. Samples that are removed from the pressure vessel but remain damp (see main text) recover some of their initial permeability. Samples that are dried before re-saturation and cycling tend to show full recovery of the initial permeability. However, higher-pressure permeability values can still be significantly lower than the permeabilities measured in cycle 1.

Finally, we note that our estimate of k is biased due to pressure sensitivity γ . We report average permeability k_{av} according to eq. (1) which assumes constant k across the sample. However, permeability is known to vary with P_e according to eq. (2) as P_p drops in the direction of flow. Solving eq. (2) for k_0 at the position in the sample where $P_p = P_0 = (P_{high} + P_{low})/2$ gives

$$k_0 = -Q\mu \frac{l}{A} \gamma [e^{\gamma\zeta/2} - e^{-\gamma\zeta/2}]^{-1} \quad (A1)$$

where $\zeta = P_{high} - P_{low}$ is the pore pressure drop across the sample. Using eqs. (1) and (A1), the bias in reported permeability can be expressed as the ratio

$$r = \frac{k_0}{k_{av}} = \frac{\gamma\zeta}{e^{\gamma\zeta/2} - e^{-\gamma\zeta/2}} \quad (A2)$$

which depends only on the product $\gamma\zeta$. In the limit as γ or ζ approach zero, k_{av} approaches k_0 . Also note that $k_{av} \geq k_0$. At high P_e , γ is small and $r \sim 0.999$. The mismatch is greatest at low P_e where γ is greatest ($0.1\text{--}0.2 \text{ MPa}^{-1}$). In this case $1 > r > 0.998$. For the values reported in this paper the bias is less than 0.2% and can be neglected.

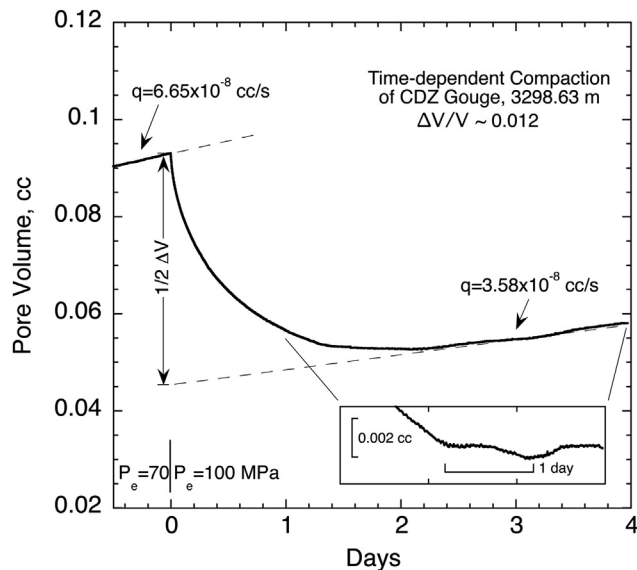


Fig. A1. Time-dependent compaction of fault gouge when effective confining pressure is increased from 70 to 100 MPa, illustrated using sample of CDZ gouge from 3298.63 m. The total inferred change in sample pore volume during this pressures step is ΔV . Inset box with an exaggerated vertical scale shows small fluid volume perturbations due to daily temperature cycles.

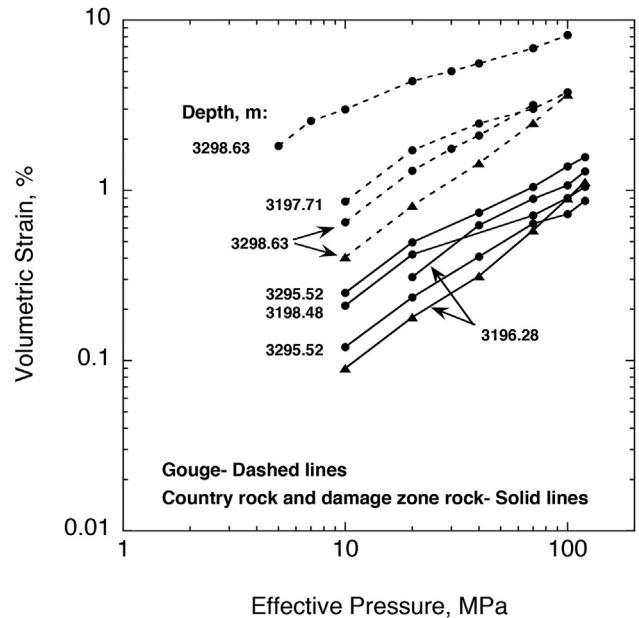


Fig. A2. Cumulative volumetric strain as a function of effective confining pressure. Gouge samples (dashed lines) experience more strain when pressurized than country rock and damage zone rock (solid lines). Two samples (3196.28 and 3298.63 m) were pressure cycled a second time (triangular data points). These second cycles show less volumetric strain.

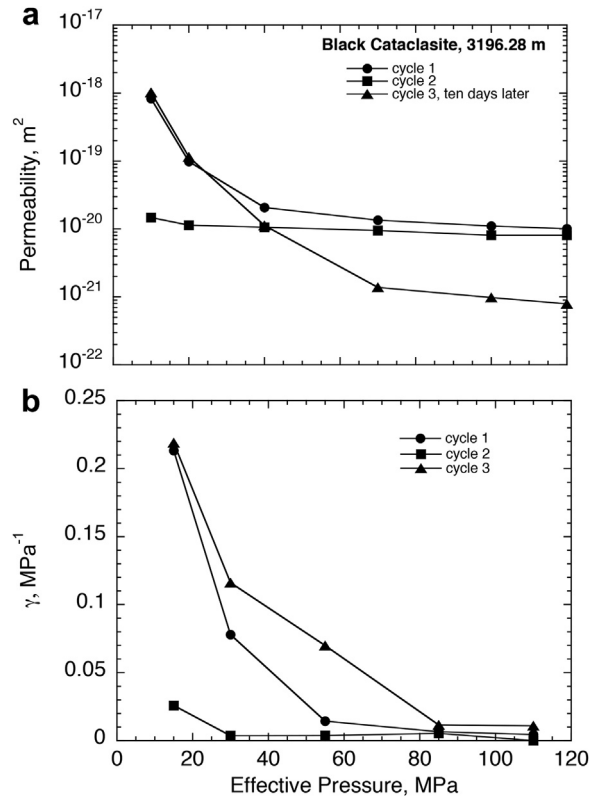


Fig. A3. a) Permeability of a black cataclasite (3196.28 m) versus effective confining pressure. Cycle 2 was conducted one day after cycle 1, while still in the pressure vessel. Cycle 3 was conducted 10 days later after bench drying. b) Pressure sensitivity coefficient γ for the three pressure cycles. In each cycle, permeability progressed from low to high effective pressure.

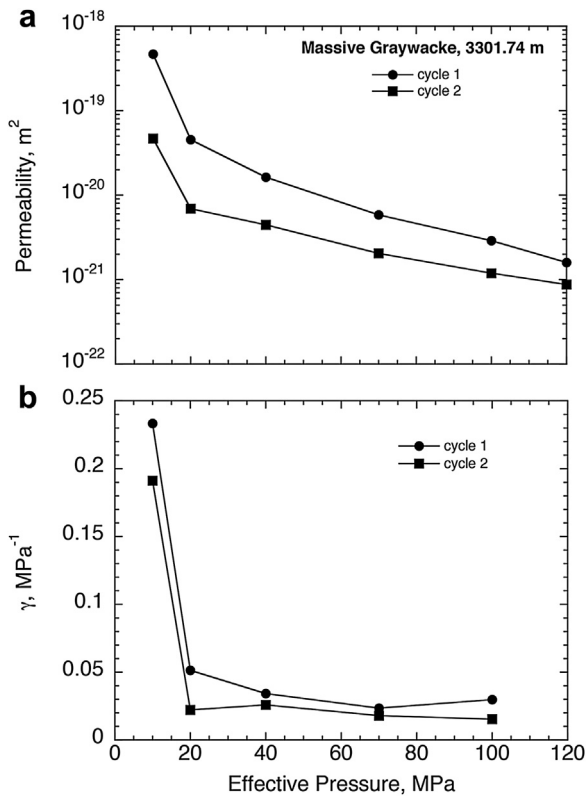


Fig. A4. a) Permeability of a massive graywacke (3301.74 m) versus effective confining pressure. Cycle 2 was conducted five months after cycle 1. b) Pressure sensitivity coefficient γ for the two cycles.

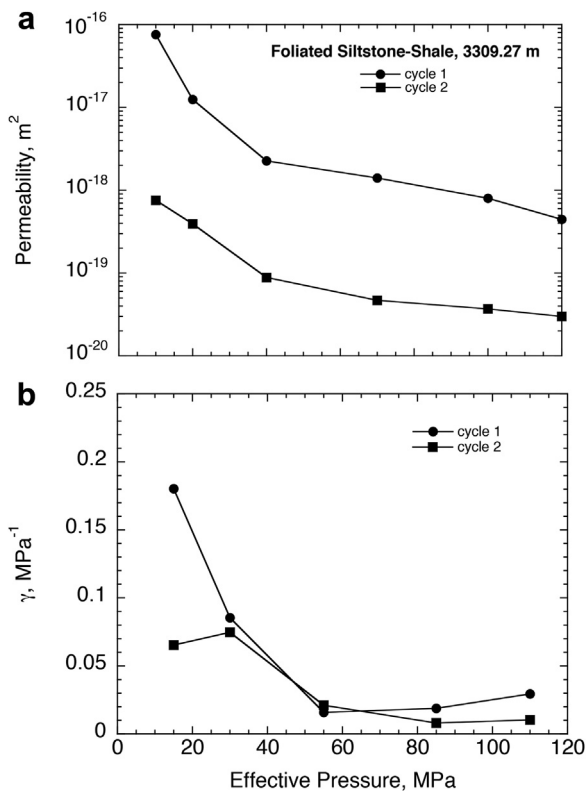


Fig. A5. a) Permeability of a foliated siltstone-shale (3309.27 m) containing vertical fractures versus effective confining pressure. Cycle 2 was conducted 3 h after cycle 1. b) Pressure sensitivity coefficient γ for the two cycles.

References

- Barton, C.A., Hickman, S., Morin, R., Zoback, M.D., Finkbeiner, T., Sass, J., Benoit, D., 1997. Fracture permeability and its relationship to in-situ stress in the Dixie Valley, Nevada, geothermal reservoir. In: Proceedings of the 22nd Workshop on Geothermal Reservoir Engineering, January 27–29, 1997. Stanford University.
- Behnen, J., Faulkner, D.R., 2011. Water and argon permeability of phyllosilicate powders under medium to high pressure. *J. Geophys. Res.* 116, B12203. <http://dx.doi.org/10.1029/2011JB008600>.
- Boness, N., Zoback, M., 2006. A multi-scale study of the mechanisms controlling shear velocity anisotropy in the San Andreas Fault Observatory at Depth. *Geophysics* 71 (5), F131–F146.
- Brace, W.F., 1980. Permeability of crystalline and argillaceous rocks. *Int. J. Rock Mech. Min. Sci. Geomech. Abstr.* 17, 241–251.
- Brune, J., Henyey, T., Roy, R., 1969. Heat flow, stress, and rate of slip along the San Andreas Fault. *J. Geophys. Res.* 74, 3821–3827.
- Bradbury, K.K., Evans, J.P., Chester, J.S., Chester, F.M., Kirschner, D.L., 2011. Lithology and internal structure of the San Andreas Fault at depth based on characterization of Phase 3 whole-rock core in the San Andreas Observatory at Depth (SAFOD) borehole. *Earth Planet. Sci. Lett.* 310, 131–144. <http://dx.doi.org/10.1016/j.epsl.2011.07.020>.
- Byerlee, J., 1990. Friction, overpressure and fault normal compression. *Geophys. Res. Lett.* 17, 4741–4750.
- Caine, J., Evans, J., Forster, C., 1996. Fault zone architecture and permeability structure. *Geology* 24 (11), 1025–1028.
- Caine, J., Bruhn, R., Forster, C., 2010. Internal structure, fault rocks and inferences regarding deformation, fluid flow, and mineralization in the seismogenic Stillwater normal fault, Dixie Valley, Nevada. *J. Struct. Geol.* 32, 1576–1589.
- Carpenter, B., Marone, C., Saffer, D., 2011. Weakness of the San Andreas Fault revealed by samples from the active fault zone. *Nature Geosci.* 4, 251–254.
- Carpenter, B., Saffer, D., Marone, C., 2012. Frictional properties and sliding stability of the San Andreas Fault from deep drill core. *Geology* 40, 759–762. <http://dx.doi.org/10.1130/G33007.1>.
- Chery, J., Zoback, M.D., Hickman, S., 2004. A mechanical model of the San Andreas Fault and SAFOD Pilot Hole stress measurements. *Geophys. Res. Lett.* 31 (15), L15513.
- Chester, F., Logan, J., 1987. Composite planar fabric of gouge from the Punchbowl Fault, California. *J. Struct. Geol.* 9 (5/6), 621–634.
- Chester, J.S., Chester, F.M., Sills, D.W., Heron, B., Almeida, R.V., 2010. Structure of the San Andreas Fault at SAFOD. *Eos Trans. AGU* 91. Fall Meeting Supplement, Abstract T52B-03.
- Ellsworth, W.L., Malin, P.E., 2011. Deep rock damage in the San Andreas Fault revealed by P- and S-type fault-zone-guided waves. In: Fagereng, A., Toy, V.G., Rowland, J.V. (Eds.), *Geology of the Earthquake Source: A Volume in Honour of Rick Sibson*, vol. 359. Geological Society, London, Special Publications, pp. 39–53.
- Faulkner, D., Rutter, E., 2001. Can the maintenance of overpressured fluids in large strike-slip fault zones explain their apparent weakness? *Geology* 29, 503–506.
- Faulkner, D., Lewis, A., Rutter, E., 2003. On the internal structure and mechanics of large strike-slip faults: field observations from the Carboneras fault, south-eastern Spain. *Tectonophysics* 367, 235–251.
- Fulton, P., Saffer, D., Bekins, B., 2009. A critical evaluation of crustal dehydration as the cause of an overpressured and weak San Andreas Fault. *Earth Planet. Sci. Lett.* 284, 447–454.
- Hickman, S., 1991. Stress in the lithosphere and the strength of active faults. In: Shea, M.A. (Ed.), *U.S. National Report International Union Geodesy and Geophysics, 1987–1990: Contributions in Tectonophysics*. American Geophysical Union, Washington, DC, pp. 759–775.
- Hickman, S., Zoback, M., 2004. Stress orientations and magnitudes in the SAFOD pilot hole. *Geophys. Res. Lett.* 31, L15512. <http://dx.doi.org/10.1029/2004GL020043>.
- Holdsworth, R., van Diggelen, E., Spiers, C., de Bresser, J., Walter, R., Bowen, L., 2011. Fault rocks from the SAFOD core samples: implications for weakening at shallow depths along the San Andreas Fault, California. *J. Struct. Geol.* 33, 132–144. <http://dx.doi.org/10.1016/j.jsg.2010.11.010>.
- Inoue, A., Utada, M., 1991. Smectite-to-chlorite transformation in thermally metamorphosed volcanoclastic rock in the Kamikita area, northern Honshu, Japan. *Am. Mineral.* 76, 628–640.
- Janssen, C., Worth, R., Reinicke, A., Rybacki, E., Naumann, R., Wenk, H.-R., Dresen, G., 2010. Nanoscale porosity in SAFOD core samples (San Andreas Fault). *Earth Planet. Sci. Lett.* 301, 179–189. <http://dx.doi.org/10.1016/j.epsl.2010.10.040>.
- Lachenbruch, A.H., Sass, J.H., 1980. Heat flow and energetics of the San Andreas Fault Zone. *J. Geophys. Res.* 85 (11), 6185–6223.
- Lachenbruch, A.H., Sass, J.H., 1992. Heat flow from Cajon Pass, fault strength and tectonic implications. *J. Geophys. Res.* 97 (B4), 4995–5015. <http://dx.doi.org/10.1029/91JB01506>.
- Lockner, D.A., Tanaka, H., Ito, H., Ikeda, R., Omura, K., Naka, H., 2009. Geometry of the Nojima fault at Nojima-Hirabayashi, Japan. I. A simple damage structure inferred from borehole core permeability. *Pure Appl. Geophys.* 166. <http://dx.doi.org/10.1007/s00024-00009-00515-00020>.
- Lockner, D., Morrow, C., Moore, D., Hickman, S., 2011. Low strength of deep San Andreas Fault gouge from SAFOD core. *Nature* 472, 82–85.
- Mase, C., Smith, L., 1987. Effects of frictional heating on the thermal, hydrological, and mechanical response of a fault. *J. Geophys. Res.* 92, 6249–6272.

- Moore, D.E., Lockner, D.A., 2004. Crystallographic controls on the frictional behavior of dry and water-saturated sheet structure minerals. *J. Geophys. Res.* 109, B03401. <http://dx.doi.org/10.1029/2003JB002508>.
- Moore, D.E., Lockner, D.A., 2007. Friction of the smectite clay montmorillonite: a review and interpretation of data. In: Dixon, T.H., Moore, C. (Eds.), *The Seismogenic Zone of Subduction Thrust Faults, MARGINS Theoretical Experimental Earth Science Series*, vol. 2. Columbia Univ. Press, New York, pp. 317–345.
- Moore, D.E., Rymer, M.J., 2012. Correlation of clayey gouge in a surface exposure of serpentinite in the San Andreas Fault with gouge from the San Andreas Fault Observatory at Depth (SAFOD). *J. Struct. Geol.* 38, 51–60. <http://dx.doi.org/10.1016/j.jsg.2011.11.014>.
- Mori, Y., Nishiyama, T., Yanagi, T., 2007. Chemical mass balance in a reaction zone between serpentinite and metapelites in the Nishisonogi metamorphic rocks, Kyushu, Japan: implications for devolatilization. *Island Arc* 16, 28–39.
- Morrow, C.A., Lockner, D.A., 1997. Permeability and porosity of the Illinois UPH 3 drillhole granite and a comparison with other deep drillhole rocks. *J. Geophys. Res.* 102, 3067–3075.
- Morrow, C.A., Shi, L.Q., Byerlee, J.D., 1984. Permeability of fault gouge under confining pressure and shear stress. *J. Geophys. Res.* 89, 3193–3200.
- Morrow, C.A., Moore, D.E., Lockner, D.A., 2000. The effect of mineral bond strength and adsorbed water on fault gouge frictional strength. *Geophys. Res. Lett.* 27, 815–818.
- Mount, V., Suppe, J., 1987. State of stress near the San Andres Fault: implications for wrench tectonics. *Geology* 15, 1143–1146.
- Rathbun, A., Fry, M., Kitajima, H., Song, I., Carpenter, B., Marone, C., Saffer, D., 2012. Permeability of the San Andreas Fault core and damage zone from SAFOD drill core. *Eos Trans. AGU*, 2012 Fall Meeting Supplemental.
- Rice, J., 1992. Fault stress states, pore pressure distributions, and the weakness of the San Andreas Fault. In: Evans, B., Wong, T.-f. (Eds.), *Fault Mechanics and Transport Properties of Rocks*. Academic Press, San Diego, CA, pp. 69–88.
- Sanford, R.F., 1982. Growth of ultramafic reaction zones in greenschist to amphibolite-facies metamorphism. *Am. J. Sci.* 282, 543–616.
- Sibson, R., 1992. Implications of fault valve behavior for rupture nucleation and recurrence. In: Mikumo, et al. (Eds.), *Earthquake Source Physics and Earthquake Precursors*. Tectonophysics 211, 283–293.
- Sills, D.W., 2010. The Fabric of Clasts, Veins and Foliations within the Actively Creeping Zones of the San Andreas Fault at SAFOD: Implications for Deformation Processes. MS thesis. Texas A&M University.
- Sills, D.W., Chester, J.S., Chester, F.M., 2009. Shape preferred orientation of porphyroclasts in the active gouge zones of the San Andreas Fault at SAFOD. *Eos Trans. AGU* 90 (52), Fall Meeting Supplemental, Abstract T43A-2057.
- Sleep, N.H., Blanpied, M.L., 1992. Creep, compaction and the weak rheology of major faults. *Nature* 359, 687–692.
- Tembe, S., Lockner, D., Wong, T.-f., 2010. Effect of clay content and mineralogy on frictional sliding behavior of simulated gouges: binary and ternary mixtures of quartz, illite, and montmorillonite. *J. Geophys. Res.* 115 (B03416). <http://dx.doi.org/10.1029/2009JB006383>.
- Tembe, S., Lockner, D., Wong, T.-f., 2009. Constraints on the stress state of the San Andreas Fault with analysis based on core and cuttings from San Andreas Observatory at Depth (SAFOD) drilling phases 1 and 2. *J. Geophys. Res.* 114. <http://dx.doi.org/10.1029/2008JB005883>.
- Wang, C.-Y., 2011. High pore pressure, or its absence, in the San Andreas Fault. *Geology* 39 (11), 1047–1050.
- Wibberley, C., Shimamoto, T., 2003. Internal structure and permeability of major strike-slip fault zones: the Median Tectonic Line in Mie Prefecture, Southwest Japan. *J. Struct. Geol.* 25 (1), 59–78. [http://dx.doi.org/10.1016/S0191-8141\(02\)00014-7](http://dx.doi.org/10.1016/S0191-8141(02)00014-7).
- Wiersberg, T., Erzinger, J., 2008. Origin and spatial distribution of gas at seismogenic depths of the San Andreas Fault from drill-mud gas analysis. *Appl. Geochem.* 23, 1675–1690.
- Wiersberg, T., Erzinger, J., 2011. Chemical and isotope compositions of drilling mud gas from the San Andreas Fault Observatory at Depth (SAFOD) boreholes: implications on gas migration and the permeability structure of the San Andreas Fault. *Chem. Geol.* 284, 148–159. <http://dx.doi.org/10.1016/j.chemge.2011.02.016>.
- Wong, T.-f., Zhu, W., 1999. Brittle faulting and permeability evolution: hydromechanical measurement, microstructural observation, and network modeling. In: Haneberg, S., et al. (Eds.), *Faults and Subsurface Fluid Flow in the Shallow Crust*, Geophysical Monograph Series, vol. 113. AGU, Washington, DC.
- Zhang, S., Tullis, T.E., Scruggs, V.J., 1999. Permeability anisotropy and pressure dependency of permeability in experimentally sheared gouge materials. *J. Struct. Geol.* 21, 795–806.
- Zoback, M., et al., 1987. New evidence for the state of stress on the San Andreas Fault system. *Science* 238, 1105–1111.
- Zoback, M., Hickman, S., Ellsworth, W., 2010. Scientific drilling into the San Andreas Fault zone. *Eos Trans. AGU* 91 (22), 197–204.
- Zoback, M., Hickman, S., Ellsworth, W., 2011. Scientific drilling into the San Andreas Fault zone – an overview of SAFOD's first five years. *Sci. Drill.* 11, 14–28.